



HAL
open science

Paleoenvironmental evolution of Picos de Europa (Spain) during marine isotopic stages 5c to 3 combining glacial reconstruction, cave sedimentology and paleontological findings

Daniel Ballesteros, Adrián Álvarez-Vena, Mael Monod-del Dago, Laura Rodríguez-Rodríguez, Jorge Sanjurjo-Sánchez, Diego Álvarez-Lao, Carlos Pérez-Mejías, Pablo Valenzuela, Irene Defelipe, César Laplana, et al.

► To cite this version:

Daniel Ballesteros, Adrián Álvarez-Vena, Mael Monod-del Dago, Laura Rodríguez-Rodríguez, Jorge Sanjurjo-Sánchez, et al.. Paleoenvironmental evolution of Picos de Europa (Spain) during marine isotopic stages 5c to 3 combining glacial reconstruction, cave sedimentology and paleontological findings. *Quaternary Science Reviews*, 2020, 248, pp.106581 -. 10.1016/j.quascirev.2020.106581 . hal-03493365

HAL Id: hal-03493365

<https://hal.science/hal-03493365v1>

Submitted on 17 Oct 2022

HAL is a multi-disciplinary open access archive for the deposit and dissemination of scientific research documents, whether they are published or not. The documents may come from teaching and research institutions in France or abroad, or from public or private research centers.

L'archive ouverte pluridisciplinaire **HAL**, est destinée au dépôt et à la diffusion de documents scientifiques de niveau recherche, publiés ou non, émanant des établissements d'enseignement et de recherche français ou étrangers, des laboratoires publics ou privés.



Distributed under a Creative Commons Attribution - NonCommercial 4.0 International License

1 **Paleoenvironmental evolution of Picos de Europa (Spain) during Marine Isotopic Stages 5c to 3**
2 **combining glacial reconstruction, cave sedimentology and paleontological findings.**

3 Daniel Ballesteros (1), Adrián Álvarez-Vena (2), Mael Monod-Del Dago (3), Laura Rodríguez-
4 Rodríguez (4, 5), Jorge Sanjurjo-Sánchez (6), Diego Álvarez-Lao (2), Carlos Pérez-Mejías (7), Pablo
5 Valenzuela (8), Irene DeFelipe (9), César Laplana (10), Hai Cheng (7), Montserrat Jiménez-Sánchez
6 (2).

7 (1) UMR 6266 - IDEES, University of Rouen-Normandie/CNRS. Mont Saint-Aignan CEDEX, France.
8 daniel.ballesteros@univ-rouen.fr

9 (2) Department of Geology, University of Oviedo. c/ Jesús Arias de Velasco s/n, 33005, Oviedo.
10 adrian@picos-europa.com, dalao@geol.uniovi.es, mjimenez@geol.uniovi.es

11 (3) Université Paris 1 Panthéon-Sorbonne, 191 rue Saint Jacques, 75005 Paris. maelmdd@gmail.com

12 (4) Laboratoire de Géographie Physique (UMR 8591, CNRS). 1 Place Aristide Briand, 92195 Meudon
13 CEDEX, France. lelydriguez@gmail.com

14 (5) Departamento de Ciencias de la Tierra y Física de la Materia Condensada, Universidad de
15 Cantabria. Avenida de los Castros 48, 39005 Santander, Spain

16 (6) University Institute of Geology Isidro Parga Pondal, University of A Coruña. Campus de Elviña s/n,
17 15011, A Coruña, Spain. jsanjurjo@udc.es

18 (7) Institute of Global Environmental Change, Xi'an Jiaotong University, Xi'an, 710049, China.
19 perezmegias@mail.xjtu.edu.cn, cheng021@xjtu.edu.cn.

20 (8) TRAGSATEC S.A. c/ Julián Camarillo 6B, 28037, Madrid, Spain.
21 pablo.valenzuela.mendizabal@gmail.com

22 (9) Geosciences Barcelona (CSIC). c/ Lluís Solé i Sabaris s/n 08028 Barcelona.
23 irene.defelipe@gmail.com

24 (10) Museo Arqueológico Regional de la Comunidad de Madrid. Pza. Bernardas s/n, 28801, Alcalá de
25 Henares, Spain. cesar.laplana@gmail.com

26 **ABSTRACT**

27 In glaciated areas, the environmental evolution before MIS 2 is usually poorly constrained mainly due
28 to the later glacial erosion during the global Last Glacial Maximum (LGM). However, in carbonate
29 areas, karst caves can preserve records of pre-LGM paleoenvironment interest. We studied a cave

30 (1350 m altitude) to establish the paleoenvironmental evolution of a glaciated karst area in Picos de
31 Europa (SW Europe). For this objective, a glacial reconstruction, cave sedimentology analyses,
32 macro- and micromammal remains are combined with ten U-Th, OSL and AMS ¹⁴C ages. The paleo-
33 glacial reconstruction indicates glaciers descended down to 810–1040 m of altitude covering an area
34 in 36.18 km² of the surroundings of Covadonga Lakes during the glacial local maximum, with the
35 equilibrium line altitude located at 1524 ± 36 m. The geomorphological study of the cave and the U-Th
36 and OSL dates reveal the presence of three allochthonous alluvial sediment sequences at 132-135,
37 98-60 and ca. 36 ka. These last two sequences would come from the erosion of fluvio-glacial
38 sediments including teeth fragments of *Pliomys coronensis* (= *P. lenki*), an unusual species in NW
39 Spain in high areas during the Upper Pleistocene. In addition, found remains of chamois (*Rupicapra*
40 *pyrenaica*) dated in 37–33 cal ka BP constitutes the oldest evidence of chamois above 800 m asl in
41 the region. All the presented data indicate the development of alpine glacier-free areas covered by
42 fluvio-glacial sediments at ca. 1450 m altitude at 98-60 and 37–33 ka, corresponding to glacial retreat
43 stages.

44

45 **KEYWORDS**

46 Karst, glacial reconstruction, paleoenvironment, *Pliomys coronensis*, *Rupicapra pyrenaica*.

47 **1. INTRODUCTION**

48 Paleoenvironmental records corresponding to Marine Isotope Stages (MIS) 4–3 are relatively scarce in
49 glaciated mountains, mainly due to glacier erosion associated to the Last Glacial Maximum (LGM) of
50 MIS 2. In areas made of limestone or another soluble rock, karst caves often preserve abundant
51 additional paleoenvironmental evidence sheltered from surface weathering (Häuselmann, 2013). Cave
52 evidence can be compared with surface landforms and sedimentary logs in order to reconstruct the
53 past environmental evolution of a territory, improving our understanding on glacial advances and
54 retreats (Myroie and Myroie, 2004; Bočić et al., 2012; Weremeichik and Myroie 2014).

55 In glaciated areas, endokarst sedimentary records are mainly represented by speleothems and fluvial
56 deposits, commonly originated during the Pliocene–Upper Pleistocene (Audra et al., 2006). Among the
57 speleothems, stalagmites frequently grow during interglacial periods, when high CO₂ concentrations
58 related to warm environments favors carbonate dissolution and precipitation in the karst conduits

59 (Isola et al., 2019; Tîrlă et al., in press). However, its growth is not only limited to interglacials, as can
60 be seen in a compilation of stalagmite records from Western Europe (Lechleitner et al., 2018). During
61 glaciations, glacial melting often affects karst aquifers favoring coarse grain sedimentation or erosion
62 processes according to glacial evolution. Pioneering works by Ford (1971, 1979) and Glover (1977)
63 already established that main endokarst detrital aggradation episodes are coeval with glacial retreats
64 and, occasionally, with the onset of glacial advances. Glaciers can inject sediments in cave passages
65 located at more than 1 km depth in glaciated areas (Audra et al., 2002), as well as in shallow caves
66 influenced by glacial outwash and located at distances of over 1000 km from the icefield (Myroie,
67 1984). Since these sediments result from the glacial erosion of limestone, they are mostly formed of
68 carbonate-rich silt, the so-called “glacial rock-flour” or “glacial milk” (Bočić et al., 2012; Weremeichik
69 and Myroie, 2014). In addition, cave detrital aggradation may also include allochthonous cobbles and
70 gravels derived from the erosion of any lithology outcropping in the catchment area (Audra et al.,
71 2002; Ballesteros et al., 2017). In temperate settings, glacial valley incision dominantly occurs during
72 glaciations (Häuselmann et al., 2007). Therefore, the increase of hydraulic gradients in the endokarst
73 favours the development of torrential water flow that broadly erodes and evacuates cave sediments,
74 simultaneously to the general enlargement of previous vadose canyons (Plan et al., 2009; Adamson et
75 al., 2014). However, if glaciers reach the bottom of fluvial valleys, karst springs can be blocked by till,
76 thus triggering inundations in the endokarst (Skoglund et al., 2010). During these floods, glacial
77 carbonate silt decants forming rhythmic slackwater deposits related to sedimentary changes in
78 underground lakes (Weremeichik and Myroie, 2014; Ballesteros et al., 2017).

79 In the NW of Spain, Picos de Europa is an outstanding location worldwide to study glaciokarst
80 processes and more deeply explore the potential of cave archives as records for paleoenvironmental
81 changes, since Picos de Europa combines outstanding glaciokarst landforms (Smart, 1986) with the
82 largest cluster of deep caves worldwide (Ballesteros et al., 2019a). This study focuses on the
83 Covadonga Lakes and their surroundings, located in the NW of Picos de Europa, a reference location
84 for glacial and karst research (e.g. Rodríguez-Rodríguez et al., 2014; Serrano et al., 2017; Telbisz et
85 al., 2019). Gale and Hoare (1997) and Alonso (1998) elaborated glacial reconstruction studies and
86 Jiménez-Sánchez and Farias (2002) concluded that the local Glacial Maximum (local GM) took place
87 ca. 20 ka before the global LGM, proposing a subsequent phase of generalized glacier retreat. Later,
88 Moreno et al. (2010) established the regional paleoenvironmental evolution since 38 ka based on the

89 Enol Lake record and geomorphological evidence, and Jiménez-Sánchez et al. (2013) refined the age
90 of the local GM at ca. 45 ka. Likewise, Nieuwendam et al. (2016) studied periglacial processes during
91 late MIS 3 and Ruiz-Fernández et al. (2016) reconstructed the timing of the last deglaciation.
92 Regarding to karst studies, Ballesteros et al. (2015, 2017, 2019b) defined the Quaternary landscape
93 evolution of the area based on cave geomorphology and geochronology.
94 Nevertheless, the environmental evolution of the Covadonga Lakes area before 45 ka remains mostly
95 unknown, especially regarding to ancient fauna that remains virtually unexplored. The present study is
96 focused on the karst cave named Hayéu l'Osu with the aim to establish the paleoenvironmental
97 evolution of the Western Massif of Picos de Europa during MIS 5c–3. To achieve this goal, we carried
98 out a multidisciplinary work combining glacial reconstruction based on field evidence, speleothem U-
99 Th dating, cave detrital sediment analyses and OSL dating, and the identification of micro- and
100 macromammal remains dated by AMS radiocarbon.

101 **2. SETTING**

102 Picos de Europa National Park (NW of Spain) is a high mountainous area up to 2650 m above sea
103 level (asl), located in the northern slope of the Cantabrian Mountains (Figure 1). Picos de Europa is
104 divided in three massifs (Western, Central and Eastern) by deep fluvial gorges. The main rocks that
105 crop out are Carboniferous limestone and, secondly, Ordovician, Carboniferous and Permian–Triassic
106 sandstone and shale (Merino-Tomé et al., 2013). The climate of Picos de Europa is humid and
107 temperate with fresh summers and without a dry season (Dfb and Dfc following the Köppen
108 classification). The annual precipitation ranges from 1000 to 1800 mm and is distributed throughout
109 the year, whilst the average air temperature ranges between -3 and 17°C. Snow is present around 6–9
110 months per year above 1500 m altitude.

111 Picos de Europa is one of the most relevant karst areas worldwide, since it contains 14% of the
112 deepest caves (>1 km deep) in the world (Ballesteros et al., 2019a). The karst evolution was
113 controlled by river incision and past glaciations (Smart, 1986). Fluvial incision created narrow gorges
114 up to 2 km in depth, conditioning the development of at least 3700 caves summing a total documented
115 length of 420 km, which were most likely formed during the Pliocene and Quaternary (Figure 1C;
116 Ballesteros et al., 2015, 2019b). Cave detrital infill came from the erosion of the above-mentioned
117 nearby bedrock outcrops (Fernández-Gibert et al., 2000; Smart 1986). During the Upper Pleistocene,
118 glaciers reached their local GM extent, occupying ca. 190 km² and with their fronts descending down

119 to 600–900 m altitude (Figure 1C; Serrano et al., 2017). In the study area (Figure 2) glaciers flowed
120 below 1300 m altitude in the surroundings of Covadonga Lakes around 109–95 ka (MIS 5d–c) leading
121 to slackwater sedimentation in caves (Ballesteros et al., 2017). Later, glacial fronts reached at least
122 900 m altitude (Gale and Hoare, 1997; Alonso 1998; Moreno et al., 2010), defining a local maximum at
123 45 ± 3 ka (Jiménez-Sánchez et al., 2013). Glacier fronts retreated since ca. 45 ka, being already
124 located at ca. 1000 m elevation at 39 ka, coeval to the development of the Covadonga Lakes (Moreno
125 et al., 2010; Nieuwendam et al., 2016). According to these authors, this retreat continued during MIS
126 3, taking place under cold, dry and open conditions until 18 ka, coeval with the occurrence of
127 periglacial processes recorded by the Belbin kame deposit (Figure 2; Ruiz-Fernández et al., 2016).
128 Nevertheless, sporadic forest surrounded Picos de Europe during MIS 3 (Uzquiano et al., 2016).
129 Finally, an advance of the glacier front up to similar altitudes than the local maximum is reported at ca.
130 23–19 ka, which is ascribed to the global LGM (Ruiz-Fernández et al., 2016; Serrano et al., 2017).

131 **3. METHODOLOGY**

132 The methodology combines geomorphological, paleontological and geochronological analyses,
133 including: (1) paleo-glacier reconstruction; (2) cave geomorphology; (3) paleontological identification of
134 the remains, (4) speleothem U-Th dating, (5) detrital cave sediment OSL dating, and (4) radiocarbon
135 dating of macromammal remains. All the spatial information was managed using the Geographical
136 Information System ArcGIS (ESRI), involving topographic contours, orthophotographies and
137 topographic digital models from the Spanish National Institute of Geography (www.cnig.es; last access
138 on April 2019).

139 **3.1 Paleo-glacier reconstruction**

140 Paleo-glacier topography was reconstructed in the study area (Figure 2) for the local GM stage based
141 on geomorphological evidence compiled in Ballesteros et al. (2015, 2019b) and bed topography
142 information. Terminal moraines, glacial arêtes and cirques were used to infer the location of former
143 glacier margins during the local GM stage. Glacier topography was interpolated from 25 theoretical ice
144 surface profiles reconstructed comprising the routing pathways followed by glacier tongues along the
145 valleys and inferred from geomorphological indicators of glacier flow direction. Theoretical ice surface
146 profiles were adjusted following the methods explained in Benn and Hulton (2010), using the GlaRe
147 toolbox for ArcGIS (Pellitero et al., 2016). Basal shear stress values up to 80–120 KPa were needed to

148 adjust the theoretical ice surface profiles to existing geomorphological evidence, which are consistent
149 with those observed in modern glaciers (50 to 150 KPa; Pellitero et al., 2016). The shape factor of the
150 valley was calculated for 62 cross sections to account for the topographic controls of glacial valley
151 shape on the basal shear stress. Once reconstructed, the digital elevation model of the former glacier
152 topography was used to estimate the Equilibrium Line Altitude (ELA) in steady-state conditions
153 through the Area Altitude Ratio Balance Ratio (AABR) method of Osmaston (2005) using the ELA
154 toolbox (Pellitero et al., 2015). We consider a range of balance ratio values of 1.9 ± 0.8 representative
155 for maritime glacier datasets (Rea, 2009).

156 **3.2 Cave geomorphology**

157 We studied the geomorphology of Hayéu l'Osu Cave in order to establish its development and its
158 sedimentary infill. To achieve this, we carried out the topographic survey in collaboration with
159 speleological groups and the geomorphological mapping of the cavity at 1:100 scale. The cave survey
160 and geomorphological map were developed in ArcGIS following the procedure described in
161 Ballesteros et al. (2015). The cave survey was delineated by means of 569 stations distributed along
162 the cave conduits and 608 measurements of distance, direction and inclination between stations using
163 a DistoX rangefinder, including the vertical and horizontal diameter of the conduit at each station.
164 These measurements were analyzed using the Compass software. Later, the geomorphological map
165 was drawn projecting cave forms and deposits on the cave survey.

166 **3.3 Paleontological analyses**

167 To search for micromammal remains, four samples of detrital sediments (named HAY-07, HAY-08,
168 HAY-09 and HAY-10) summing up to ~90 kg were collected from alluvial sequences of Hayéu l'Osu
169 Cave.. Samples were water-screened using two superimposed sieves of 2- and 0.5-mm mesh size.
170 Sieves were not previously used preventing hypothetical contamination from previous samples in the
171 laboratory. Fine sieved samples was examined using a parallel-optics type stereo microscope Nikon
172 SMZ800N under 10x magnification. Photographs were taken with a 5 Mpx resolution digital camera,
173 and image orientation correction was done with Adobe Photoshop CC software. We used teeth
174 samples of current fauna as a comparison material to identify the micromammal remains found in the
175 study cave. The reference material used belongs to *Arvicola monticola*, *Microtus lavernedii*, *Microtus*
176 *lusitanicus* and *Clethrionomys glareolus*, all of them collected from *Tyto alba* pellets in the Cantabrian

177 Region, as well as MIS 3 fossil material of *Pliomys coronensis* (= *P. lenki*) recovered from the nearby
178 archeological site of La Güelga Cave (Figure 1C).

179 Macromammals were discovered by speleologists from Grupo Espelológico Polifemo (Oviedo) and
180 collaborators. Macro remains were recovered using the archaeological methodology, mapping their
181 occurrence on the geomorphological map (section 3.2). These remains were prepared for taxonomic
182 and taphonomic analyses by removing physically the silt and clay attached to the bones and
183 consolidating the samples with Paraloid B-72. Finally, we calculated the Minimum Number of
184 Individuals (MNI) of each species taking into account each skeletal element. The fossils are stored in
185 the Department of Geology at the University of Oviedo (Spain).

186 **3.4 U-Th dating**

187 Three flowstone samples from the study cave were dated by U decay series. Supplementary Data
188 (Figure S1) includes the geomorphological sections of the sampled flowstones. All samples were
189 collected in-situ with the aid of a hammer and a chisel, and drilled in the laboratory using a hand drill to
190 extract 0.1-0.2 g of carbonate powder, which was treated and analyzed at the Xi'an Jiaotong
191 University (China), following the procedures described in Edwards et al. (1987). Each sample was
192 dissolved with HNO₃ and spiked with a ²²⁹Th – ²³³U – ²³⁶U carrier solution. Once the Fe solution and
193 the ammonium hydroxide is added, the separation of U and Th was carried out using column
194 chromatography with an anion exchange resin. Finally, U and Th fractions were analyzed in a
195 multicollector-inductively coupled plasma mass spectrometer (MC-ICP-MS) ThermoFisher Neptune
196 Plus using U decay constants reported in Cheng et al. (2013). The ages are expressed in years before
197 present (BP) with their 2σ uncertainty.

198 **3.5 OSL dating**

199 Optically stimulated luminescence (OSL) dating was applied to date endokarst detrital sediments. We
200 collected five samples from sandy layers recognized in the cave stratigraphic sections detailed in
201 Supplementary Data (Figure S2). Samples were taken driving opaque PVC tubes (550 mm diameter,
202 4 mm wall) in sandy material and then carefully covered with aluminum foil immediately after
203 extraction. Samples were processed in the luminescence laboratory of the Institute of Geology Isidro
204 Parga Pondal, University of A Coruña (Spain). Under red light conditions, sand materials stored within
205 the tubes were dried and sieved. The grain fraction 180–250 μm was dried at 45°C and treated with

206 HCl and H₂O₂ in order to remove carbonates and organic matter, respectively, which constituted 65–
207 90% of the samples. Furthermore, a centrifugation step adding a high-density solution was needed to
208 separate quartz from feldspar and heavy minerals. Later, a HF dilution was used on the quartz-rich
209 fraction to obtain pure quartz. Infrared Stimulated Luminescence (IRSL) was used to verify quartz
210 purity at the end of sample treatment.

211 OSL signals were recorded using an automated RISØ TL/OSL-DA-15 reader equipped with a
212 photomultiplier EMI 9635 QA (PMT) and a ⁹⁰Sr/⁹⁰Y source (dose of 0.120 ± 0.003 Gy·s⁻¹). An optical 6
213 mm-thick Hoya U-340 filter was placed between the aliquots and the PMT to measure the UV range
214 emission. The Single Aliquot Regeneration (SAR) protocol (Murray and Wintle, 2000) was applied on
215 multigrain aliquots to estimate the equivalent Dose (D_e), considering the Central Age Model (Galbraith
216 et al., 1999) to date each sample. Frequency histograms of D_e of samples HAY-07, 09, 10 and 11 are
217 included in Supplementary Data (Figure S3). Sample HAY-08 is not included because of its low
218 reliability (only 4 aliquots) but its age is consistent with other OSL datings. Preheat tests were
219 previously performed and dose recovery tests used on bleached aliquots (Murray and Wintle, 2003).

220 The activity concentration of radioisotopes (⁴⁰K, and ²³⁸U, ²³⁵U and ²³²Th decay chains) was estimated
221 using low background gamma-ray spectrometry. Measurements of calcined and grinded sediments
222 were performed in a coaxial Canberra XTRA gamma detector (Ge Intrinsic) model GR6022 within a 10
223 cm-thick lead shield. The alpha dose-rate was neglected due to the HF etching step, and the beta
224 dose-rate corrected (Brennan, 2003). The cosmic dose-rate was estimated following Prescott and
225 Hutton (1994) and using the conversion factors proposed by Guerin et al. (2011). Resultant OSL ages
226 are expressed in years before present (BP) with their corresponding 2σ uncertainty.

227 **3.6 Radiocarbon dating**

228 Two samples from macromammal bones were sampled for radiocarbon dating through accelerator
229 mass spectrometry (AMS). Radiocarbon measurements (reference order 13274/18) were performed at
230 the Poznan Radiocarbon Laboratory, Poland. The obtained ages were calibrated using the software
231 OxCal v.4.3.2 (Bronk Ramsey, 2017) against the INTCAL 13 curve (Reimer et al., 2013), considering
232 the 2σ standard deviation (95.4% probability). The calibrations are included in Supplementary Data
233 (Figure S4) and calibrated dates are expressed in cal ka BP.

234 **4. RESULTS**

235 **4.1 Paleo-glacier reconstruction**

236 Glaciers formed an ice field in the surroundings of Covadonga Lakes during the local GM, occupying a
237 total surface extent of 36.18 km² and covering the entrance of Hayéu l'Osu Cave (Figure 3). Glacier
238 tongues reached total lengths of ca. 2 km along the valleys of Ordiales, Hunhumia, and Pomperi; up to
239 9.5 km along El Bricial–Vega de Enol valleys; 5.9 km along Ercina valley; and 6.6 km along the former
240 Belbín glacier. Glacier fronts were placed at ca. 1040 m altitude in the Ordiales, Hunhumia and Ercina
241 valleys; 925–1030 m in the El Bricial–Vega de Enol valleys; and 810 m in Belbín (Figure 3). Glacier
242 maximum thickness reached up to 105–220 m along the El Bricial–Vega de Enol valleys, 170 m along
243 the Belbín flow line, 170 m along Ercina valley, and between ca. 114 and 168 m along the valleys
244 Ordiales, Hunhumia, and Pomperi. The steady-state ELA was most likely set at 1524 ± 36 m (Figure
245 3).

246 **4.2 Cave geomorphology**

247 The Hayéu l'Osu Cave is mainly formed by a 1.6 km-long conduit (named Stream Gallery) slightly
248 tilted towards the SE, and by vertical conduits summing up to 135 m in depth (Figure 4A). Vertical
249 conduits connect the Stream Gallery and the topographic surface as shown in the cave longitudinal
250 profile (Figure 4B). Geomorphological evidence includes alluvial deposits, breakdown deposits,
251 speleothems and slackwater deposits. Alluvial sediments up to 3 m thick are present along the Stream
252 Gallery (Supplementary Data, Figure S2), involving active channel and terrace deposits. Active
253 channel deposits are located along the cave stream (Figure 4C) and resulted from the erosion of
254 terrace deposits placed at the bottom and walls of the NW of the study cave (Figures 4D and 5A–E).
255 Terrace deposits are perched up to 20 m above the streambed and are occasionally covered by
256 flowstones and stalagmites (Figure 4E). Active channel deposits and most terrace deposits are grain-
257 supported and contain sub-angular to rounded calcareous pebbles and cobbles, containing no matrix
258 or with 5–20% of sandy matrix (70–85% of carbonate and 15–30% of quartz). Both deposits comprise
259 also sub-rounded allochthonous pebbles and cobbles of sandstone, bauxite and diabase. In addition,
260 alluvial sand (70–95% of carbonate and 5–30% of quartz) form also minor terraces or constitute layers
261 interbedded within the pebble and cobble deposits. These sand deposits may eventually contain
262 micromammal remains, which have been identified and described in detail in section 4.3. Breakdown
263 deposits are common along the study cave, including angular calcareous boulders less than 2 m in
264 diameter formed by rock fall processes. Regarding the speleothems, they commonly appear in cave

265 passages perched above the cave stream. Flowstone up to 3 m thick and stalagmites less than 2 m
266 height occasionally precipitated on top of alluvial and breakdown deposits, however, flowstones
267 covered by sandy terrace deposits were also recognized. Finally, slackwater deposits show 0.5–3 m of
268 laminated silt and clay (Figure 4F) deposited essentially in the central part of the study cave (Figure
269 4A). These deposits would be related to cave floods similar to what has been observed in the nearby
270 Torca La Texa shaft (Figure 2; Ballesteros et al., 2017).

271 **4.3 Paleontology of mammal bones**

272 Seven fragments of arvicoline molars and one fragment of a rodent incisor were found in samples from
273 HAY-7, 8 and 9, collected in the Stream Gallery (Figure 4A). These remains show dentine removal by
274 erosion and four of them show also rounded edges. The best-preserved fragment corresponds to a
275 complete enamel prism found in sample HAY-9. When comparing this fragment with the upper first
276 molars of extinct and living arvicolines from the Cantabrian Region (Figure 5), its size and angle in
277 occlusal view (Figure 5a') matches with the morphology of an upper first or second molar (Figure 5b'–
278 e'). The curvature of the anterior side of the triangle at the tooth's base indicates that it belongs to a
279 rooted molar (Figure 5a''), clearly different respect to ever-growing molars (Figure 5D, E and F). All
280 these mentioned morphological features and the absence of curvature at the basal part of the
281 posterior side of the prism (Figure 5a''), match with the morphology of the buccal salient angle 3
282 (BSA3) of the first upper molar (M¹). Among the arvicolines from the Upper Pleistocene of the Iberian
283 Peninsula, only two species bear rooted molars. One of them is *P. coronensis* (Figure 5B), a very
284 common vole in rocky environments during MIS 3 and earlier before its extinction during MIS 2 in the
285 Cantabrian Region, territory that constituted the last refuge for this species before its complete
286 disappearance (Cuenca-Bescós et al., 2010). The other rooted-molar species is *C. glareolus* (Figure
287 5C), which currently inhabits the well-developed forests of the Cantabrian Region and other Eurasian
288 areas, but which is absent in alpine environments. Considering the compared morphology and the
289 chronological context (defined in section 4.4), the enamel fragment of HAY-9 has been ascribed to the
290 species *P. coronensis*. There is another enamel fragment at HAY-7 whose morphological features at
291 its basal part indicate it belongs to a rooted molar, but no further identification can be done due to its
292 poor preservation.

293

294 A total amount of 81 macromammal remains, all of them corresponding to small-sized bovids, were
295 recovered from two sites named Llamaeyu and Stream galleries (Figure 4). In Llamaeyu Gallery,
296 radius, metacarpals, phalanxes, skull fragments, vertebrae, ribs, one molar and other bones were
297 found without anatomic connection on top of a breakdown deposit (Figure 6A) whereas, in the Stream
298 Gallery, a scapula was located on a detrital deposit (Figure 6B). Morphology and morphometry of teeth
299 and skeletal elements are distinctive of chamois (Figure 7), so they are ascribed to *Rupicapra*
300 *pyrenaica* (a comprehensive discussion about the specific attribution of Upper Pleistocene chamois
301 from the Iberian Peninsula is provided by Álvarez-Lao, 2014). This fossil assemblage corresponds to a
302 minimum of four individuals (MNI): two young and two adults. The lack of anthropic activity signs
303 excludes humans as responsible for the bone accumulation. In general, no carnivore marks are
304 detected, suggesting that the bone accumulation was related to a natural trap. Only one bone shows
305 teeth marks (Figure 7D) produced by a small carnivore, most likely due to scavenging rather than
306 predation. In addition, only one bone (corresponding to one of the young individuals) shows erosion
307 features due to transportation by water (Figure 7C). From an environmental perspective, occurrence of
308 *R. pyrenaica*, a typical alpine ungulate, at Hayéu l'Osu Cave is consistent with the current rocky
309 mountain landscape of the area. Moreover, presence of a herbivore mammal in this cave clearly
310 indicates ice-free conditions in the near surroundings during the time they lived (Álvarez-Lao, 2014).

311 **4.4 Geochronology**

312 Three speleothem samples from the study cave were analyzed using U-Th dating (Table 1). Samples
313 exhibit ^{238}U content lower than 100 ppb and high initial $\delta^{234}\text{U}$ (1000-3000 ppm). Standard procedures
314 to correct the ages assume an initial $^{230}\text{Th}/^{232}\text{Th}$ atomic ratio of $4.4 \pm 2.2 \cdot 10^{-6}$ (Edwards et al., 1987;
315 Cheng et al., 2013) and the obtained ages are considered reliable.. Sample HAY-12 (263 ± 18 ka)
316 corresponds to the base of an overturned set of flowstones and stalagmites, originally precipitated on
317 top of slackwater deposits (Figure 8A). The age provided for HAY-12 represents a minimum age for
318 the slackwater deposits, which would have been decanted by cave flooding before 263 ± 18 ka, during
319 the Middle Pleistocene. Subsequently, the slackwater deposits were eroded causing the collapse of
320 the overlying flowstones and stalagmites. Similarly, samples HAY-06 (132 ± 1 ka) and HAY-13 ($135 \pm$
321 7 ka) have precipitated fossilizing fluvial deposits (Figure 8B and C), which were eroded later in the
322 case of HAY-06. Both datings indicate the occurrence of a first alluvial sequence older than 135-132
323 ka, probably during MIS 6.

324 In the study cave, five alluvial deposits described in section 4.2 were dated using OSL from 84 ± 10 to
325 36 ± 3 ka (Table 2, Figure 8C-G). The estimated dose-rates were very low due to the low radioisotope
326 content, being below 1 Gy ka^{-1} for most samples. No disequilibrium is observed in the U and Th decay
327 chains. The OSL signals were dim but fast, and provided poor signal to background ratios, causing the
328 rejection of a high number of aliquots, being the number of accepted aliquots between 4 and 35. The
329 D_e distributions were non-skewed and the over dispersion (Table 2) of the mean of the Central Age
330 Model was low, showing no evidence of incomplete bleaching of the alluvial sand grains before they
331 were introduced into the cave. Thus, the Central Age Model was used for assessing the OSL ages.
332 After bleaching, the quartz was for a short period on the topographical surface before being introduced
333 into the study cave. We consider this time to be short since the study cave is located in a hill that
334 probably acted as a by-pass area to lower zones where widespread glacial and fluvio-glacial
335 sedimentation took place (Figures 2 and 3). However, reworking processes are not totally discarded.
336 The chronological framework provided allows us to define two alluvial sequences occurring after the
337 first alluvial sequence identified by U-Th dates. According to this, a second alluvial sequence
338 corresponds to terrace sediments deposited between 84 ± 10 and 65 ± 16 ka, ranging from MIS 5c to
339 MIS 4 (Figure 8C-F), while a third sequence includes a fluvial terrace formed at 36 ± 3 ka during MIS
340 3a (Figure 8G).
341 The chronology of the second and third alluvial sequences provides the chronological framework of
342 the arvicoline remains, while the radiocarbon dates represent the timing of the chamois. A fragment
343 of metatarsal from Llamaeyu Gallery has an AMS ^{14}C age of 36 ± 1 cal ka BP whilst the scapula
344 recovered in Stream Gallery provided an age of 34.5 ± 0.6 cal ka BP (Table 3).

345 **5. DISCUSSION: PALEOENVIRONMENTAL EVOLUTION**

346 Cave geomorphology and U-Th ages provide new data about the origin and evolution of the Hayéu
347 l'Osu Cave during the Middle Pleistocene (Figure 9). Flowstone ages suggest that the cave was
348 formed prior to 263 ka (Figure 9A), like most karst cavities studied in Picos de Europa (Smart, 1986;
349 Ballesteros et al., 2015, 2019). Since its origin, Hayéu l'Osu Cave has undergone inundations that
350 would be related to Middle Pleistocene glaciations, followed by speleothem precipitation at 263 ± 18
351 ka (MIS 8). Other studies have documented coeval breccia cementation in surficial talus deposits in
352 Puertos de Áliva (Villa et al., 2013), between the Central and Eastern massifs of Picos de Europa
353 (Figure 1C). Later, at the end of MIS 6, flowstone precipitation took place in the cave at 135-132 ka,

354 covering the first alluvial sequence previously deposited. All these speleothems and detrital sediments
355 partially filled the Hayéu l'Osu Cave, as occurred in other nearby caves named Pozu Lluçia and Torca
356 La Texa (Figure 2; Ballesteros et al., 2019).

357 The paleoenvironmental evolution of the surroundings of Covadonga Lakes during MIS 5c-3 is
358 established based on the combination of geomorphological-stratigraphical and paleontological data
359 and kernel density functions (Figure 10) of U-Th, OSL and radiocarbon ages obtained in the cave. This
360 probability analysis considered also previous datings carried out in Enol lacustrine sediments by
361 Moreno et al. (2010) and in Vega de Comeya border polje by Jiménez-Sánchez et al. (2013). Four
362 phases have been distinguished (Table 4 and Figure 11) according to the probabilistic distribution of
363 Figure 10.

364 **5.1 Phase 1 (98-60 ka; MIS 5c-4)**

365 The first phase described for the study area ranges between ca. 98 and 60 ka (Figure 11A). After
366 glacial advances recorded during MIS 5cd, dated in the Central Cantabrian Mountains at 114 ± 7 ka
367 based on *in situ* produced cosmogenic nuclide ^{10}Be (Figure 1B; Rodríguez-Rodríguez et al., 2016), a
368 glacial retreat episode occurred in the study area during MIS 5c-4. In Hayéu l'Osu Cave this episode
369 might correspond to the sedimentation of the second alluvial sequence that includes *P. coronensis*.
370 Alluvial deposits are dominated by carbonate sand and silt (section 4.2), coming from the glacial
371 erosion of Carboniferous limestone, while pebbles and cobbles of sandstone and diabase were
372 eroded from sandstone and igneous dyke outcrops located in higher areas of the Western Massif of
373 Picos de Europa (Ballesteros et al., 2017, 2019b). Thus, the Ercina glacier that flowed from the
374 summit areas elevated more than 2000 m altitude of the Western Massif (Figure 3) eroded the
375 limestone, sandstone and diabase bedrock and transported the resulting sediment load to the glacier
376 fronts located higher than 1400 m altitude (Figure 11A). Sediments were probably transported by
377 glacial meltwater to the surroundings of the study cave, in a fluvio-glacial environment inhabited by *P.*
378 *coronensis*. The roundness of sediment particles observed in the alluvial sequence (section 4.2) as
379 well as in the enamel remains discovered in the study cave (section 4.3) are both compatible with this
380 interpretation. Finally, the presence of *P. coronensis* indicates that bedrock was exposed near the
381 cave under relatively cold conditions, and hence, the glacier advance was less extensive than the
382 local GM extent.

383 The sediments of the second alluvial sequence might have formed during MIS 5d glaciation identified
384 directly in the central Cantabrian Mountains (Figure 1B; Rodríguez-Rodríguez et al., 2016) and
385 indirectly in the nearby Torca La Texa shaft (Figure 2; Ballesteros et al., 2017). The decantation of
386 glacial origin rhythmite in this shaft (located at 1350 m elevation) at 109-95 ka suggests that the Ercina
387 glacier front was at around 1350-1400 m at the beginning of phase 1.

388 **5.2 Phase 2 (48–42 ka; MIS 3c)**

389 The second phase (Figure 11B) corresponds to the local GM advance of glaciers in the study area.
390 The Vega de Comeya border polje was occupied by a proglacial lake that was being filled by
391 calcareous alluvial deposits from the south-facing slopes of the Western Massif and siliceous alluvial
392 sediments from the north-facing slopes (Jiménez-Sánchez and Farias, 2002). OSL dating yielded a
393 minimum age of 45 ± 3 ka for the onset of glacio-lacustrine sedimentation in the border polje while
394 organic remains from a sand and gravel unit placed immediately on top yielded a radiocarbon age of
395 44.1 ± 0.9 cal ka BP, constraining the age of the local GM (Jiménez-Sánchez et al., 2013). Similarly,
396 the nearby Belbín kame terrace deposit (Figure 2) yielded a minimum reference age of 36.5 ± 0.5 cal
397 ka BP for the base of its sequence and, hence, for the Belbín moraine deposition (Ruiz-Fernández et
398 al., 2016). The reconstruction of the local GM extent (section 4.1) suggests that glaciers were less
399 extensive compared to previous reconstructions proposed by Gale and Hoare (1997), but it is in
400 agreement with those developed in Alonso (1998), Serrano et al. (2017), and Ruiz-Fernández et al.
401 (2016). The reconstruction also indicates that glacier fronts descended down to $-1040-810$ m asl,
402 covering the calcareous bedrock where the Hayéu l'Osu Cave develops (Figure 11B), which was
403 located below the estimated ELA (1524 ± 36 m). The altitude of the steady-state ELA in our work is
404 consistent with previous regional ELA reconstructions made by Santos-González et al. (2013), but ca.
405 100 m lower than the mean ELA estimated in Serrano et al. (2017).

406 **5.3 Phase 3 (42-38 ka; MIS 3b)**

407 Phase 3 represents the onset of glacier retreat in the surroundings of Covadonga Lakes (Jiménez-
408 Sánchez and Farias, 2002). Glacier retreat was recorded by proglacial lacustrine sedimentation at
409 Enol Lake at 38 ± 2 cal ka BP, exposing the glacial depression now occupied by Enol Lake but with
410 the glacial front still located close to the lake and supplying ablation water and coarse inorganic
411 sediments (Moreno et al., 2010). During this phase (Figure 11C), the evolution of the Ercina glacier

412 front would have been consistent with that of El Bricial-Vega de Enol glacier recording a new episode
413 of detrital sediment infill at 39 ± 3 ka. Hence, the Ercina glacier was likely shorter at ca. 38 ka than
414 previously assumed (Moreno et al., 2010). Glacier retreat prior to 36–39 ka has also been reported in
415 Puertos de Áliva, a site located between the Central and Eastern massifs (Figure 1C; Serrano et al.,
416 2012).

417 **5.4 Phase 4 (37–33 ka; MIS 3a)**

418 Glaciers continued receding during phase 4 (Figure 11D). The Ercina glacier front had already
419 ascended well above 1400 m by 37 ka, while the third alluvial sequence was being deposited within
420 the Hayéu l'Osu Cave. The third detrital sequence is thinner and less extensive than the second
421 detrital sequence, suggesting that the volume of surface sediment was higher during MIS 5d glaciation
422 than during the local GM of MIS 3c. MIS 5d glaciation occurred after the Eemian interglacial substage,
423 when weathering processes would have been more intense than over MIS 4. Besides, the third alluvial
424 sequence deposited at 36 ± 3 ka within the study cave also involved micromammal remains.
425 Consequently, this sequence should come from fluvio-glacial sediments sourcing from the retreating
426 glacier fronts similar to the interpretation for the second alluvial sequence (section 5.1) even if minor
427 reworking processes would take place.

428 Subsequently, at least three chamois accidentally fell inside the cave. The current position of these
429 remains at 50 and 100 m depth (from the topographic surface) and the absence of evidence produced
430 by carnivores, scavengers or humans support the role of the cave as a natural trap. Only one bone
431 shows minor bite marks caused by a small carnivore (e.g. weasel, beech marten). In the Llamaeyu
432 Gallery, bone remains most likely arrived by gravity processes and minor water transport, as the fauna
433 assemblage is not in anatomic connection and is related to a breakdown deposit (section 4.2). In the
434 Stream Gallery, the chamois bone is located in a subhorizontal conduit and have been transported by
435 an underground stream after its accidental fall in the cave. The lack of transport marks recognized in
436 the bone suggests that it may have arrived protected by the soft parts of the animal.

437 The existence of chamois bones points to the presence of an alpine environment with exposure of
438 rocky areas developed under relatively cold climate at 37–33 ka. This time range coincides with a
439 relative cold period according to the NGRIP $\delta^{18}\text{O}$ ice core record (Figure 12; NGRIP, 2004).
440 Nevertheless, at a regional scale, the presence of chamois is coeval with a period of less cold
441 conditions marked by an increase in organic matter and coarse sediments in the paleolake of Puertos

442 de Áliva (1400 m altitude) between 36 and 32 ka (Serrano et al., 2012). In lower areas, the pollen
443 record of El Esquilleu Cave (Figure 1C; 350 m asl) revealed the occurrence of *Pinus* forest with minor
444 deciduous and evergreen oaks, but also heathland shrubs in the SW of Picos de Europa at around
445 38–34 ka (Uzquiano et al., 2016) that would have been part of the chamois diet.

446 During the late MIS 3, chamois constituted one of the main food sources of the Mousterian–
447 Aurignacian humans who lived in areas below 400 m elevation in the Cantabrian Mountains (Yravedra
448 and Cobo-Sánchez et al., 2015). Around Picos de Europa, archeological excavations discovered
449 abundant remains of hunted chamois in Sopeña (Pinto-Llona et al., 2012), El Esquilleu (Uzquiano et
450 al., 2012; Yravedra et al., 2014), La Güelga (Menéndez et al., 2018) and other cavities suggesting that
451 the hunting zones were located in lower areas (Figure 1C). However, the chamois remains found in
452 Hayéu l'Osu Cave indicate that the populations of this caprine could also have occupied areas of
453 Picos de Europa up to, at least, 1400 m elevation, during 37–33 ka.

454 6. CONCLUSIONS

455 We propose a new paleoenvironmental evolution model during MIS 5c–3 for Picos de Europa based
456 on a multidisciplinary work combining glacial and cave geomorphology, Quaternary paleontology and
457 geochronology on a glaciokarst area. The study of sediment records in Hayéu l'Osu Cave have
458 allowed us to constrain the timing of glacier retreat, and thus complement previous reconstructions on
459 paleo-glacier evolution in Picos de Europa. In addition, mammal remains preserved in caves are
460 exceptional indicators of glacial ice-free areas in the past, pointing out to a paleoenvironment
461 developed over successive pulses of the glacial evolution.

462 Three alluvial stratigraphic sequences have been identified in Hayéu l'Osu Cave. The first sequence
463 was deposited before 135–131 ka (MIS 6), while the second and third sequence, with micromammal
464 remains, were sedimented at 98–60 ka and ca. 36 ka respectively. Additionally, chamois remains (37–
465 33 ka) were found on top of the third sequence. This stratigraphic record suggests the development of
466 alpine ice-free areas at ca. 1400 m altitude during 98–60 ka (MIS 5c–4), when glaciers were probably
467 located at higher altitudes. Later, glaciers with a length of 9.5 km and up to 100–220 m in thickness,
468 descended down to 810–1030 m elevation during the local GM stage, establishing a proglacial lake
469 environment in the Comeya border polje at 48–42 ka (MIS 3c). Over this period, the study cave was
470 located in the glacial ablation zone and covered by glaciers. A general trend of glacier retreat occurred
471 from 42–38 ka, with the glacial fronts located above 1400 m altitude at 37–33 ka. In this setting,

472 chamois inhabited the ice-free rocky steep slopes of Picos de Europa, in agreement with a slight
473 increase in local temperature.

474 In addition, the distribution of species in the Cantabrian Region provides further insights on the
475 paleoenvironmental evolution of the study area. Remains of *P. coronensis* allow us to extend its
476 altitudinal distribution up to ca. 1400 m in the Cantabrian Region during MIS 4, whereas the chamois
477 bone assemblage of Hayéu l'Osu Cave constitutes the oldest evidence of *R. pyrenaica* above 1000 m
478 altitude of the Cantabrian Region. Chamois inhabited the highlands of Picos de Europa at 37-33 ka
479 coevally with human occupation in lower areas, who broadly hunted chamois. However, our outcomes
480 suggest that the studied chamois remains fell accidentally in Hayéu l'Osu Cave, being accumulated in
481 the stratigraphic record by natural processes without any human contribution.

482 **AUTHOR CONTRIBUTION**

483 DB, LRR and MJS conducted the research. MMD and LRR elaborated the paleo-glacier
484 reconstruction. DB performed the cave geomorphology and collected all samples in cooperation with
485 PV, IDF and the speleological team. AAV found and identified rodent remains under the guidance of
486 CL, whilst DAL studied the macromammal assemblages. JS carried out the OSL datings, and CPM
487 obtained the U-Th ages under the direction of HC. DB, LRR, DAL, AAV, IDF, PV and CPM wrote the
488 article and designed the figures. All authors have contributed to the discussion.

489 **ACKNOWLEDGEMENTS**

490 Picos de Europa National Park founded this work through the Geocancosta (FC-
491 GRUPIN6IDI/2018/000184) and FUE-300-17 projects, receiving the grateful assistance of the National
492 Park staff and the speleologists from Grupo Espeleológico Polifemo (Oviedo), GES Montañeiros
493 Celtas (Vigo), Grupo de Espeleología Diañu Burlón (Corvera de Asturias), and Espéleo Club Aradelas
494 (Vigo). LRR is grant holder of the post-doctoral Clarín-COFUND Program, financed jointly by the 7th
495 WP of the European Union–Marie Curie Actions and Gobierno del Principado de Asturias (Reference
496 ACA-17-19). We appreciate the work of Jo de Waele, Rafael López-Martínez and other reviewers.

497 **REFERENCES**

- 498 Adamson, K.R., Woodward, J.C., Hughes, P.D. 2014. Glaciers and rivers: Pleistocene uncoupling in a
499 Mediterranean mountain karst. *Quaternary Science Reviews*, 94, 28–43.
- 500 Alonso, V. 1998. Covadonga National Park (Western Massif of Picos de Europa, NW Spain): a
501 calcareous deglaciated area. *Trabajos de Geología* 20, 167–181.

502 Álvarez-Lao, D.J. 2014. The Jou Puerta Cave (Asturias, NW Spain): a MIS 3 large mammal
503 assemblage with mixture of cold and temperate elements. *Palaeogeography,*
504 *Palaeoclimatology, Palaeoecology* 393, 1–19.

505 Audra, P., Quinif, Y., Rochette, P. 2002. The genesis of Tennengerbirge karst and caves (Salzburg,
506 Austria). *Journal of Cave and Karst Studies* 64, 153–164.

507 Audra, P., Bini, A., Gabrovšek, F., Häuselmann, P., Hobléa, F., Jeannin, P.Y., Kunaver, J., Monbaron,
508 M., Šušteršič, F., Tognini, P., Trimmel, H., Wildberger, A. 2006. Cave genesis in the Alps
509 between the Miocene and today: a review. *Zeitschrift für Geomorphologie* 50, 153–176.

510 Ballesteros, D., Jiménez-Sánchez, M., Giralt, S., García-Sanseguno, J., Meléndez-Asensio, M. 2015.
511 A multi-method approach for speleogenetic research on alpine karst caves. Torca La Texa
512 shaft, Picos de Europa (Spain). *Geomorphology* 247, 35–54.

513 Ballesteros, D., Jiménez-Sánchez, M., Giralt, S., DeFelipe, I., García-Sanseguno, J. 2017. Glacial
514 origin for cave rhythmite during MIS 5d–c in a glaciokarst landscape, Picos de Europa (Spain).
515 *Geomorphology* 286, 68–77.

516 Ballesteros, D., Fernández-Martínez, E., Carcavilla, L., Jiménez-Sánchez, M. 2019a. Karst Cave
517 Geoheritage in Protected Areas: Characterisation and Proposals of Management of Deep
518 Caves in the Picos de Europa National Park (Spain). *Geoheritage* 11(4), 1919-1939..

519 Ballesteros, D., Giralt, S., García-Sanseguno, J., Jiménez-Sánchez, M. 2019b. Quaternary regional
520 evolution based on karst cave geomorphology in Picos de Europa (Atlantic Margin of the
521 Iberian Peninsula). *Geomorphology* 336, 133–151.

522 Benn, D.I., Hulton, N.R.J. 2010. An Excel™ spreadsheet program for reconstructing the surface
523 profile of former mountain glaciers and ice caps. *Computers & Geosciences* 36, 605–610.

524 Bočić, N., Faivre, S., Kovačić, M., Horvatinčić, N. 2012. Cave development under the influence of
525 Pleistocene glaciation in the Dinarides – an example from Štirovača Ice Cave (Velebit Mt.,
526 Croatia). *Zeitschrift für Geomorphologie*, 56, 409–433.

527 Bronk Ramsey, C. 2017. Methods for Summarizing Radiocarbon Datasets. *Radiocarbon* 59, 1-25.

528 Brennan, B.J. 2003. Beta doses to spherical grains. *Radiation Measurements* 3, 299–303.

529 Cheng, H., Edwards, L. R., Shen, C.-C., Polyak, V.J., Asmerom, Y., Woodhead, J., Hellstrom, J.,
530 Wang, Y., Kong, X., Spötl, C., Wang, X., Alexander, E. C. 2013. Improvements in ²³⁰Th
531 dating, ²³⁰Th and ²³⁴U half-life values, and U-Th isotopic measurements by multi-collector
532 inductively coupled plasma mass spectrometry. *Earth and Planetary Science Letters*, 371-372,
533 82-91.

534 Clark, P.U., Dyke, A.S., Shakun, J.D., Carlson, A.E, Clark, J., Wohlfarth, B., Mitrovica, J.X., Hostetler,
535 S.W., McCabe, A.M. *Science* 7, 710-714.

536 Colhoun, E.A., Kiernan, K., Barrows, T.T., Goede, A. 2010. Advances in Quaternary studies in
537 Tasmania. *Special Publications*, 346. Geological Society of London. Londres. 165–183.

538 Cuenca-Bescós, G., Straus, L. G., García-Pimienta, J. C., González Morales, M.R., López-García,
539 J.M. 2010. Late Quaternary small mammal turnover in the Cantabrian Region: The extinction of
540 *Pliomys lenki* (Rodentia, Mammalia). *Quaternary International* 212, 129–136.

541 Edwards, R.L., Chen, J.H., Wasserburg, G.J. 1987. ^{238}U , ^{234}U , ^{230}Th , ^{232}Th systematics and the precise
542 measurement of time over the past 500,000 years. *Earth and Planetary Science Letters*, 81,
543 175–192.

544 Fernández-Gibert, E., Calaforra, J.M., Rossi, C. 2000. Speleogenesis in the Picos de Europa Massif,
545 Northern Spain, in: Klimchouk, A., Ford, D., Palmer, A., Dreybrodt, W. (Eds.), *Speleogenesis:
546 Evolution of Karst Aquifers*, National Speleological Society, Huntsville, Alabama, pp. 352–357.

547 Ford, D.C. 1971. Characteristics of Limestone Solution in the Southern Rocky Mountains and Sle Kirk
548 Mountains, Alberta and British Columbia. *Canadian Journal of Earth Sciences* 8, 585–609.

549 Ford, D.C. 1979. A review of alpine karst in the southern Rocky Mountains of Canada. *National
550 Speleological Society Bulletin* 41, 53–65.

551 Galbraith, R.F., Roberts, R.G., Laslett, G.M., Yoshida, H., Olley, J.M. 1999. Optical dating of single
552 and multiple grains of quartz from Jinmium Rock Shelter, Northern Australia: Part 1,
553 Experimental design and statistical models. *Archaeometry* 41, 339–364.

554 Gale, S.J., Hoare, P.G. 1997. The glacial history of the northwest Picos de Europa of northern Spain.
555 *Zeitschrift für Geomorphologie* 41, 81–96.

556 Glover, R. R. 1977. A conceptual model of cave development in a glaciated region. *Proceedings of 7th
557 International Speleological Congress*. International Union of Speleology, Sheffield, pp. 220–
558 221.

559 Guerin, G., Mercier, N., Adamiec, G. 2011. Dose-rate conversion factors: update. *Ancient TL* 29, 5–8.

560 Häuselmann, P. 2013. Large epigenic caves in high-relief areas. In: Shroder, J., Frumkin, A. (Eds.)
561 *Treatise on Geomorphology*, Vol 6, *Karst Geomorphology*. Academic Press, San Diego, 207–
562 219.

563 Häuselmann, P., Granger, D.E., Jeannin, P.Y., Lauritzen, S.E. 2007. Abrupt glacial valley incision at
564 0.8 Ma dated from cave deposits in Switzerland. *Geology* 35, 143–146.

565 Isola, I., Ribolini, A., Zanchetta, G., Bini, M., Regattieri, E., Drysdale, R. N., Hellstrom, J.C., Bajo, P,
566 Montagna, P., Pons-Branchu, E. 2019. Speleothem U/Th age constraints for the Last Glacial
567 conditions in the Apuan Alps, northwestern Italy. *Palaeogeography, Palaeoclimatology,
568 Palaeoecology* 518, 62–71.

569 Jiménez-Sánchez, M., Farias, P. 2002. New radiometric and geomorphologic evidences of a last
570 glacial maximum older than 18 ka in SW European mountains: the example of Redes Natural
571 Park (Cantabrian Mountains, NW Spain). *Geodinamica Acta* 15, 93–101.

572 Jiménez-Sánchez, M., Rodríguez-Rodríguez, L., García-Ruiz, J.M., Domínguez-Cuesta, M.J., Farias,
573 P., Valero-Garcés, B., Moreno, A., Rico, M., Valcárcel, M. 2013. A review of glacial
574 geomorphology and chronology in northern Spain: Timing and regional variability during the
575 last glacial cycle. *Geomorphology* 196, 50–64.

576 Lechleitner, F.A., Amirnezhad-Mozhdehi, S., Columbu, A., Comas-Bru, L., Labuhn, I., Pérez-Mejías,
577 P., Rehfeld, K. 2018. The Potential of Speleothems from Western Europe as Recorders of
578 Regional Climate: A Critical Assessment of the SISAL Database. *Quaternary* 1 (3), 30.

579 Menéndez, M., Álvarez-Alonso, D., Andrés-Herrero, M. de, Carral, P., García-Sánchez, E., Jordá-
580 Pardo, J.F., Quesada, J.M., Rojo, J. 2018. The Middle to Upper Paleolithic transition in La
581 Güelga cave (Asturias, Northern Spain). *Quaternary International* 474, 71–84.

582 Merino-Tomé, O., Suárez Rodríguez, A., Alonso, J., González Menéndez, L., Heredia, N., Marcos, A.
583 2013. Mapa Geológico Digital continuo E. 1:50.000, Principado de Asturias (Zonas: 1100–
584 1000–1600) [WWW Document]. GEODE. Mapa Geológico Digital Continuo de España.
585 SIGECO-IGME. URL <http://cuarzo.igme.es/sigeco/default.htm>

586 Moreno, A., Valero-Garcés, B.L., Jiménez-Sánchez, M., Domínguez-Cuesta, M.J., Mata, M., Navas,
587 A., González-Sampériz, P., Stoll, H., Farias, P., Morello, M., Corella, J., Rico, M. 2010. The
588 last deglaciation in the Picos de Europa National Park (Cantabrian Mountains). *Journal of*
589 *Quaternary Sciences* 25, 1076–1091.

590 Murray, A.S., Wintle, A.G. 2000. Luminescence dating of quartz using an improved single-aliquot
591 regenerative-dose protocol. *Radiation Measurements* 32, 57–73.

592 Murray, A.S., Wintle, A.G. 2003. The single aliquot regenerative dose protocol: Potential for
593 improvements in reliability. *Radiation Measurements* 37, 377–381.

594 Mylroie, J.E. 1984. Pleistocene climatic variation and cave development: *Norsk Geografisk Tidsskrift*
595 38, 151–156.

596 Mylroie, J.E., Mylroie, J.R. 2004. Glaciated karst: how the Helderberg plateau revised the geological
597 perception. *Northeastern Geology and Environmental Sciences* 26, 82–92.

598 Nieuwendam, A., Ruiz-Fernández, J., Oliva, M., Lopez, V., Cruces, A., Freitas, M. da C. 2015.
599 Postglacial landscape changes and cryogenic processes in Picos de Europa (northern Spain)
600 reconstructed from geomorphological mapping and microstructures on quartz grains.
601 *Permafrost and Periglacial Processes* 27, 96–108.

602 NGRIP members 2004. High-resolution record of Northern Hemisphere climate extending into the last
603 interglacial period. *Nature* 431, 147–151.

604 Osmaston H. 2005. Estimates of glacier equilibrium line altitudes by the Area×Altitude, the
605 Area×Altitude Balance Ratio and the Area×Altitude Balance Index methods and their
606 validation. *Quaternary International* 138–139, 22–31.

607 Pellitero, R., Rea, B.R., Spagnolo, M., Bakke, J., Ivy-Ochs, S., Lukas, S., Ribolini, A. 2015. A GIS tool
608 for automatic calculation of glacier equilibrium-line altitudes. *Computers & Geosciences* 82,
609 55–62.

610 Pellitero, R., Rea, B.R., Spagnolo, M., Bakke, J., Ivy-Ochs, S., Frew, C.R., Hughes, P., Ribolini, A.,
611 Lukas, S., Renssen, H. 2016. GlaRe, a GIS tool to reconstruct the 3D surface of
612 palaeoglaciers. *Computers & Geoscience* 94, 77–85.

613 Pinto-Llona, A.C., Clark, G., Karkanias, P., Blackwell, B., Skinner, A.R., Andrews, P., Reed, K., Miller,
614 A., Macías-Rosado, R., Vakiparta, J. 2012. The Sopeña Rockshelter, a New Site in Asturias
615 (Spain) bearing evidence on the Middle and Early Upper Palaeolithic in Northern Iberia.
616 *Munibe (Antropología-Arkeología)* 63, 45–79.

617 Plan, L., Filipponi, M., Behm, M., Seebacher, R., Jeutter, P., 2009. Constraints on alpine
618 speleogenesis from cave morphology — A case study from the eastern Totes Gebirge
619 (Northern Calcareous Alps, Austria). *Geomorphology* 106, 118–129.

620 Prescott, J.R., Hutton, J.T. 1994 Cosmic ray contributions to dose rates for luminescence and ESR
621 dating: large depths and long term variations. *Radiation Measurements* 23, 497–500.

622 Railsback, L.B., Gibbard, P.L., Head, M.J., Voarintsoa, N.R.G., Toucanne, S. 2015. An optimized
623 scheme of lettered marine isotope substages for the last 1.0 million years, and the
624 climatostratigraphic nature of isotope stages and substages. *Quaternary Science Reviews*
625 111, 94–106.

626 Rea, B.R. 2009. Defining modern day Area-Altitude Balance Ratios (AABRs) and their use in glacier-
627 climate reconstructions. *Quaternary Science Review* 28, 237–248.

628 Reimer, P., Bard, E., Bayliss, A., Beck, J.W., Blackwell, P., Ramsey, C.B., Buck, C., Cheng, H.,
629 Edwards, R.L., Friedrich, M., Grootes, P.M., Guilderson, T.P., Hafliðason, H., Hajdas, I.,
630 Hatt_e, C., Heaton, T.J., Hoffmann, D.L., Hogg, A.G., Hughen, K., Kaiser, K.F., Kromer, B.,
631 Manning, S.W., Niu, M., Reimer, R.W., Richards, D.A., Scott, E.M., Southon, J., Staff, R.A.,
632 Turney, C.S.M., Van der Plicht, J. 2013. Intcal13 and Marine13 radiocarbon age calibration
633 curves 0–50,000 years cal BP. *Radiocarbon* 55, 1869–1887.

634 Rodríguez-Rodríguez, L., Jiménez-Sánchez, M., Domínguez-Cuesta, M.J., Aranburu, A. 2014.
635 Research history on glacial geomorphology and geochronology of the Cantabrian Mountains,
636 north Iberia (43–42°N/7–2°W). *Quaternary International* 364, 6–21.

637 Rodríguez-Rodríguez, L., Jiménez-Sánchez, M., Domínguez-Cuesta, M.J., Rinterknecht, V., Pallàs,
638 R., Bourlès, D. 2016. Chronology of glaciations in the Cantabrian Mountains (NW Iberia)
639 during the Last Glacial Cycle based on in situ-produced ¹⁰Be. *Quaternary Science Reviews*
640 138, 31–48.

641 Ruiz-Fernández, J., Oliva, M., Cruces, A., Lopes, V., Freitas, M. da C., Andrade, C., García-
642 Hernández, C., López-Sáez, J.A., Gerales, M. 2016. Environmental evolution in the Picos de
643 Europa (Cantabrian Mountains, SW Europe) since the Last Glaciation. *Quaternary Science*
644 *Reviews* 138, 87–104.

645 Santos-González, J., Redondo-Vega, J.M., González-Gutiérrez, R.B., Gómez-Villar, A. 2013. Applying
646 the AABR method to reconstruct equilibrium-line altitudes from the last glacial maximum in the
647 Cantabrian Mountains (SW Europe). *Palaeogeography, Palaeoclimatology, Palaeoecology*
648 387, 185–199.

649 Serrano, E., González-Trueba, J.J., González-García, M. 2012. Mountain glaciation and paleoclimate
650 reconstruction in the Picos de Europa (Iberian Peninsula, SW Europe). *Quaternary Research*
651 78, 303–314.

652 Serrano, E., González-Trueba, J.J., Pellitero, R., Gomez-Lende, M. 2017. Quaternary glacial history of
653 the Cantabrian Mountains of northern Spain: a new synthesis, in: Hughes, P.D., Woodward,
654 J.C. (Eds.), *Special Publications*, 433: *Quaternary Glaciation in the Mediterranean Mountains*,
655 Geological Society of London, London, pp. 55–85.

- 656 Skoglund, R.Ø., Lauritzen, S.E., Gabrovšek, F. 2010. The impact of glacier ice-contact and subglacial
657 hydrochemistry on evolution of maze caves: A modelling approach. *Journal of Hydrology* 388,
658 157–172.
- 659 Smart, P.L. 1986. Origin and development of glacio-karst closed depressions in the Picos de Europa,
660 Spain. *Zeitschrift für Geomorphologie* 30, 423–443.
- 661 Stuiver, M., Reimer, P.J. 1993. Extended 14C data base and revised CALIB 3.0 14C age calibration
662 program. *Radiocarbon* 35, 215–230.
- 663 Telbisz, T., Tóth, G., Ruban, D.A., Gutak, J.M. 2019. Notable glaciokarst of the World. In: Veress, M.
664 Telbisz, T., Tóth, G., Lózy, D., Ruban, D.A., Gutak, J.M. (Eds), *Glaciokarst*. Springer, Cham,
665 373–499.
- 666 Tîrlă, L., Drăgușin, V., Bajo, P., Covaliov, S., Cruceru, N., Ersek, V., Hanganu, D., Hellstrom, J.,
667 Hoffmann, D., Mirea, I., Sava, T., Sava, G., Șandric, I. In press. Quaternary environmental
668 evolution in the South Carpathians reconstructed from glaciokarst geomorphology and
669 sedimentary archives. *Geomorphology*, 354: 107038.
- 670 Uzquiano, P., Yravedra, J., Ruiz Zapata, B., Gil García, M.J., Sesé, C., Baena, J. 2012. Human
671 behaviour and adaptations to MIS 3 environmental trends (>53–30 ka BP) at Esquilleu cave
672 (Cantabria, northern Spain). *Quaternary International* 252, 82–89.
- 673 Uzquiano, P., Ruiz-Zapata, M.B., Gil-García, M.J., Fernández, S., Carrion, J.S. 2016. Late Quaternary
674 developments of Mediterranean oaks in the Atlantic domain of the Iberian Peninsula: The case
675 of the Cantabrian region (N Spain). *Quaternary Science Reviews* 153, 63–77.
- 676 Villa, E., Stoll, H., Farias, P., Adrados, L., Edwards, R.L., Cheng, H. 2013. Age and significance of the
677 Quaternary cemented deposits of the Duje Valley (Picos de Europa, Northern Spain),
678 *Quaternary Research* 79, 1-5.
- 679 Weremeichik, J., Mylroie, J. 2014. Glacial Lake Schoharie: an investigative study of glaciolacustrine
680 lithofacies in caves, Helderberg Plateau, Central New York. *Journal of Cave and Karst Studies*
681 76, 127–138.
- 682 Yravedra, J., Gómez-Castanedo, A., Aramendi Picado, J., Baena Preysler, J. 2014. Specialised
683 hunting of Iberian ibex during Neanderthal occupation at El Esquilleu Cave, northern Spain.
684 *Antiquity* 88, 1035–1049.
- 685 Yravedra, J., Cobo-Sánchez, L. 2015. Neanderthal exploitation of ibex and chamois in southwestern
686 Europe. *Journal of Human Evolution* 78, 12–32.

687 **FIGURE CAPTIONS**

688 Figure 1. (A) Map of the SW of Europe with the location of Picos de Europa (northern Spain). (B) DEM
689 of the N of Spain including the local Maximum Ice Extent (local MIE) recorded by former glaciers in the
690 Cantabrian Mountains (Rodríguez-Rodríguez et al., 2014). (C) DEM of the three massifs of Picos de
691 Europa with the position of the study cave (named Hayéu l’Osu) in the surroundings of Covadonga
692 Lakes (Enol and Ercina lakes), within the NW massif. Local glacial maximum (Local GM) extent

693 according to Alonso (1998), Serrano et al. (2012, 2017) and Rodríguez-Rodríguez et al. (2014).
694 Documented cave data is courtesy of the speleological groups reported in Ballesteros et al. (2019a).
695 Figure 2. Main geomorphological features of the study area (which position is shown in Figure 1)
696 projected on the hillshade digital model. Geomorphology is after Ballesteros et al. (2015, 2017,
697 2019b), who studied the Pozu Lluçia and Torca La Texa shafts.
698 Figure 3. (A) Aerial photo of the Spanish PNOA 2017 Program projected on a digital elevation model
699 of the Western Massif of Picos de Europa (www.cnig.es; last accessed on May 2019); the star marks
700 the location of Hayéu l'Osu Cave. (B) Topographic restitution of glaciers for the local GM stage,
701 showing the location of the Equilibrium Line Altitude (ELA) and the main ice flow pathways: 1-
702 Ordiales, 2-Hunhumia, 3-Pomperi, 4-El Bricial (4'-Vega de Enol), 5-Ercina, and 6-Belbín.
703 Figure 4. (A) Geomorphological map of Hayéu l'Osu Cave showing the location of the paleontological
704 sites, the position of dating samples and pictures shown in C, D, E and F. (B) Cave longitudinal profile
705 (P indicates the depth of each shaft in meters, from its top to bottom). (C) Vadose canyon of Stream
706 Gallery showing active channel deposits. (D) Camp Chamber dominated by fluvial terrace deposits.
707 (E) Vadose canyon of Stream Gallery showing fluvial terrace deposits cemented by flowstone and
708 perched above the active channel. (F) Slackwater deposits from the central part of the cavity.
709 Figure 5. Comparison of the enamel fragment from the Stream Gallery of the Hayéu l'Osu Cave
710 (Figure 4A) with the upper first molars of some extinct and living arvicolines from the Cantabrian
711 Region. Squares in occlusal view (a'-f') are highlighting the buccal salient angle 3 (BSA3). Squares in
712 buccal view (a''-f'') are highlighting the morphology at the base of the BSA3. (A) Enamel fragment
713 found in HAY-9 sample from the study cave. (B) Rooted molars of *Pliomys coronensis* from La Güelga
714 Cave (Figure 1C). (C) Rooted molar of *Clethrionomys glareolus*. Evergrowing molars of: (D) *Arvicola*
715 *monticola*, (E) *Microtus lavernedii*, and (F) *Microtus lusitanicus*.
716 Figure 6. Chamois (*Rupicapra pyrenaica*) sites from Hayéu l'Osu Cave: (A) Debris deposit with bone
717 remains (Figure 7A and C-K) in the Llamaeyu Gallery (Figure 4). (B) Location of a scapula (Figure 7B)
718 placed on alluvial deposits of the Stream Gallery (Figure 4).
719 Figure 7. Chamois (*Rupicapra pyrenaica*) dental and postcranial remains from Hayéu l'Osu Cave. (A)
720 Left M³ in labial view. (B) Young left scapula in lateral view. (C) Fragment of limb bone diaphysis
721 showing erosion due to transportation by water. (D) Young left radius diaphysis in anterior view
722 showing teeth marks (indicated by white arrows) produced by a small carnivore. (E) Adult right

723 metacarpal in anterior view. (F) Young left metacarpal in anterior view. (G) Adult proximal phalanx in
724 anterior view. (H) Adult middle phalanx in anterior view. (I) Adult distal phalanx in lateral view. (J) Adult
725 right calcaneus in anterior view. (K) Adult right talus in anterior view. Scale bars are in cm.

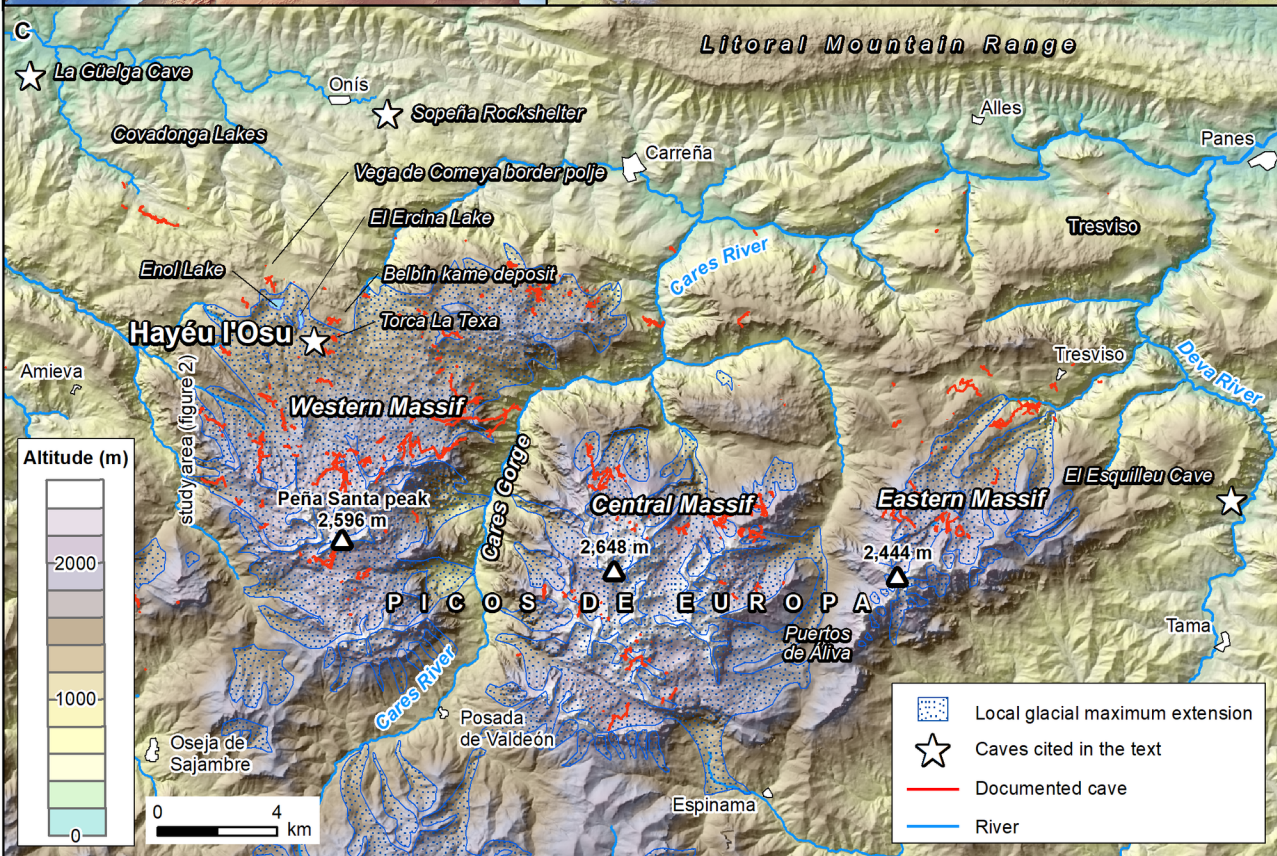
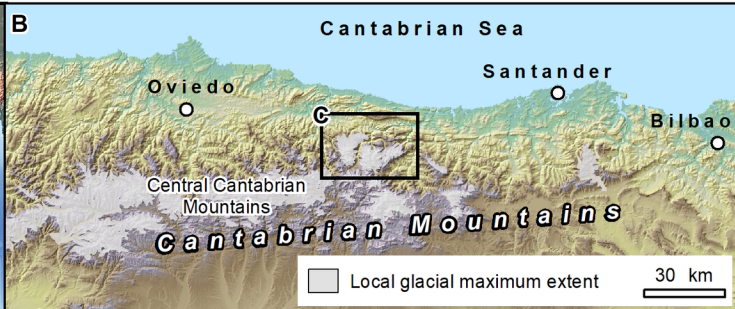
726 Figure 8. Selected sites of Hayéu l'Oosu Cave for U-Th and OSL dating: (A) Toppled stalagmite and
727 flowstone originally located on top of slackwater deposits which were subsequently eroded after 263
728 ka. (B) Perched flowstone precipitated on a first alluvial sequence. (C, D) Second alluvial sequence
729 deposited on flowstone. (E) Second alluvial sequence covered by speleothems. (F) Zoom of sandy
730 layers dated through OSL. (G) Third alluvial pebble sequence with a sandy layer interbedded and
731 dated by means of OSL. Picture locations are shown in Figures 4A and 8.

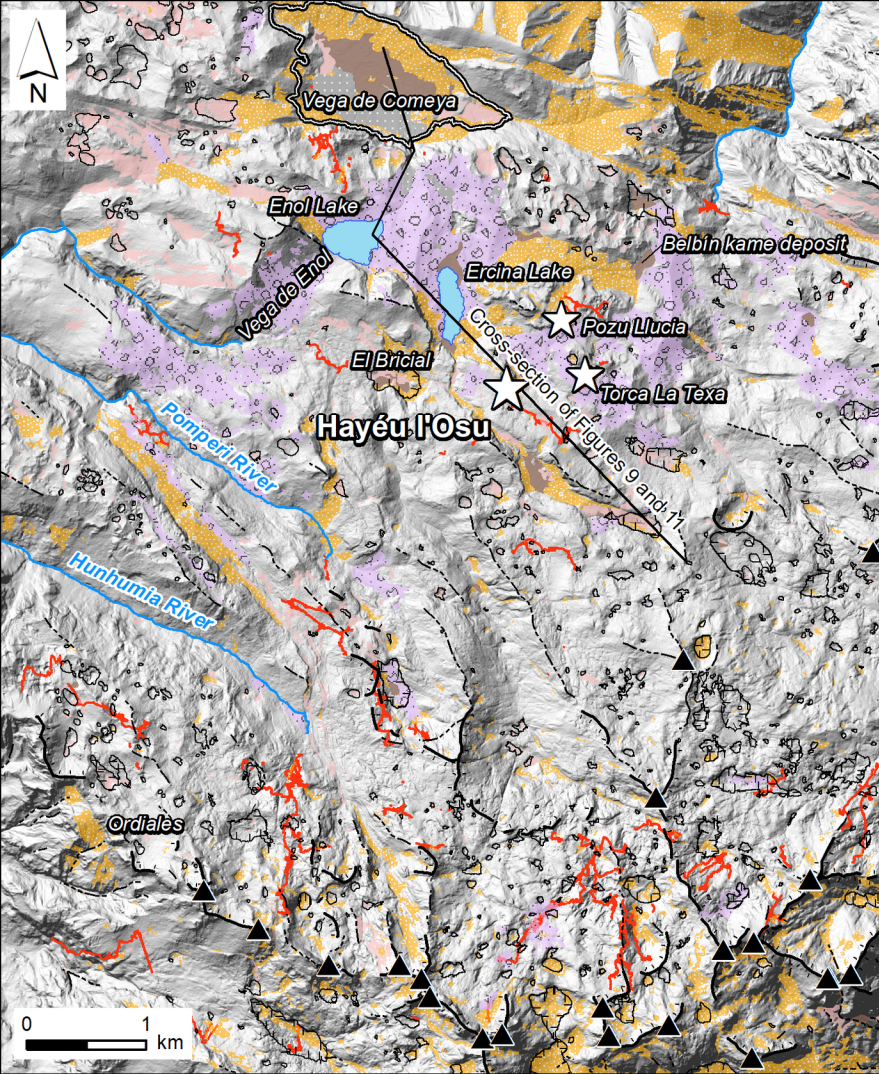
732 Figure 9. Cross-section of the surroundings of Covadonga Lakes showing the position of Hayéu l'Oosu
733 Cave, Enol and Ercina lakes and Vega de Comeya border polje, which sedimentary infill was
734 previously described and dated in Jiménez-Sánchez and Farias (2002). The position of the cross-
735 section is shown in Figure 2. Bedrock geology is based on Ballesteros et al. (2015). Dates performed
736 in Hayéu l'Oosu Cave are detailed in Tables 1, 2 and 3.

737 Figure 10. Kernel density functions of the OSL, U-Th and radiocarbon ages obtained in the Hayéu
738 l'Oosu Cave record, including previous ages from the Vega de Comeya and Enol lacustrine sediments
739 (Moreno et al., 2009; Jiménez-Sánchez et al., 2013). Flowstone precipitation ascribable to the end of
740 MIS 6 fossilized the first detrital sequence identified inside the study cave. The second important
741 episode of cave sediment infill occurred between ca. 98 and 60 ka (phase 1) as glacio-fluvial
742 sediments from a previous glaciation (most likely MIS 5d glaciation) were washed into the cave. The
743 Vega de Comeya sequence indicates that the local Glacial Maximum (local GM) was attained in this
744 area around 45 ± 3 ka (Jiménez-Sánchez et al., 2013), during MIS 3c (phase 2, 48–42 ka). By ~38 ka
745 BP glaciers had already retreated from the Enol Lake depression, allowing proglacial lacustrine
746 sedimentation (Moreno et al., 2010). The retreat of the Ercina glacier front is indirectly recorded in
747 Hayéu l'Oosu Cave by the third sedimentary sequence (phase 3, 42–38 ka), suggesting that the Ercina
748 glacier front had also suffered considerable retreat from its previous GM position. The cave entrance
749 and its neighboring areas remained ice-free (phase 4) after ca. 37 ka until, at least, the glacier
750 advance linked to the global LGM of MIS 2 whose extent remains unknown in Picos de Europa (LGM
751 age interval according to Clark et al., 2009).




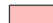


752 Figure 11. Paleoenvironmental evolution of the Covadonga Lakes surroundings during MIS 5d–3a
753 illustrated using the cross-section shown in Figure 8 (same legend; see Figure 2 for cross-section
754 location). (A) Phase 1: the study cave recorded detrital sediment input at 98–60 ka, evidencing that
755 the cave setting was an ice-free alpine environment and that eventual glacial fronts were located
756 above 1400 m altitude. (B) Phase 2: glaciers attained their local GM extent at 45 ± 3 ka, causing
757 proglacial lacustrine sedimentation at Vega de Comeya (Jiménez-Sánchez et al., 2013). The Ercina
758 glacier flowed down to 1040 m asl, and La Picota moraine was formed between Ercina and Enol
759 glaciers (Moreno et al., 2010). (C) Phase 3: onset of a general trend of glacial retreat according to
760 Jiménez-Sánchez and Farias (2002). Glaciers receded from the Enol Lake depression at ca. 38 cal ka
761 BP, while Hayéu l'Osu Cave recorded detrital sedimentation since 36 ± 3 ka (HAY-7). (D) Phase 4:
762 occurrence of ice-free temperate environment inhabited by chamois populations.

763 Figure 12. AMS radiocarbon dates of chamois remains from Llamaeyu and Stream galleries of Hayéu
764 l'Osu Cave, projected over the Greenland $\delta^{18}\text{O}$ ice core record (NGRIP, 2004). MIS 3 substages
765 according to Railsback et al. (2015).














Karst features

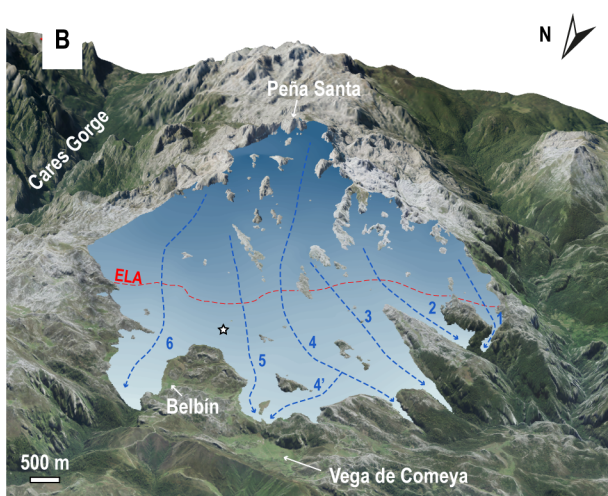
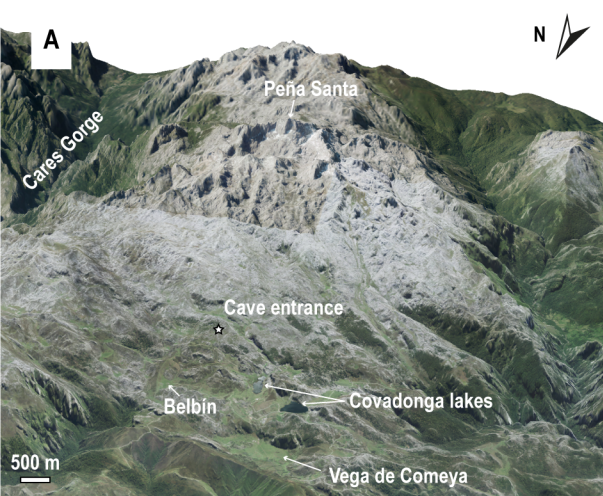
-  Study cave
-  Previous studied caves
-  Doline (> 400 m²)
-  Karst soils and sediments
-  Cave conduit
-  Border *polje*

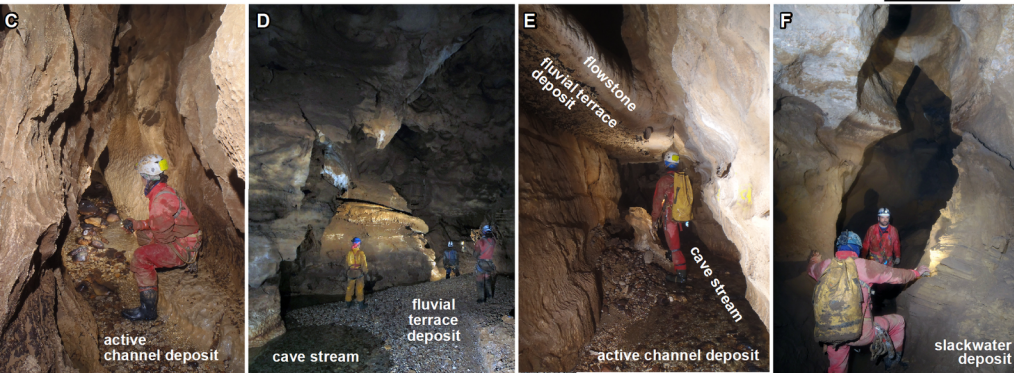
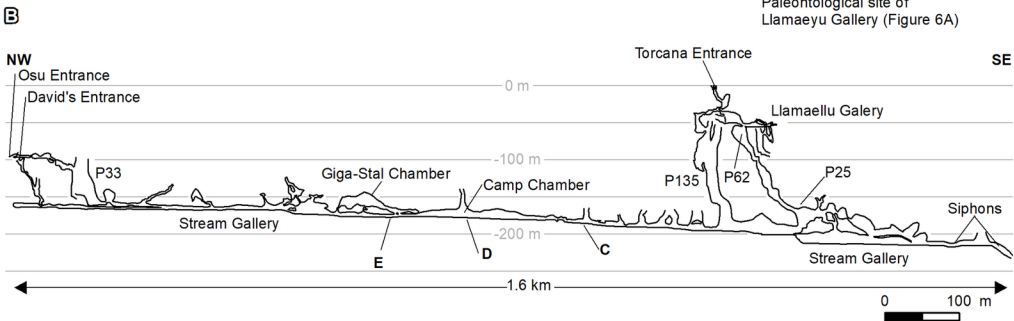
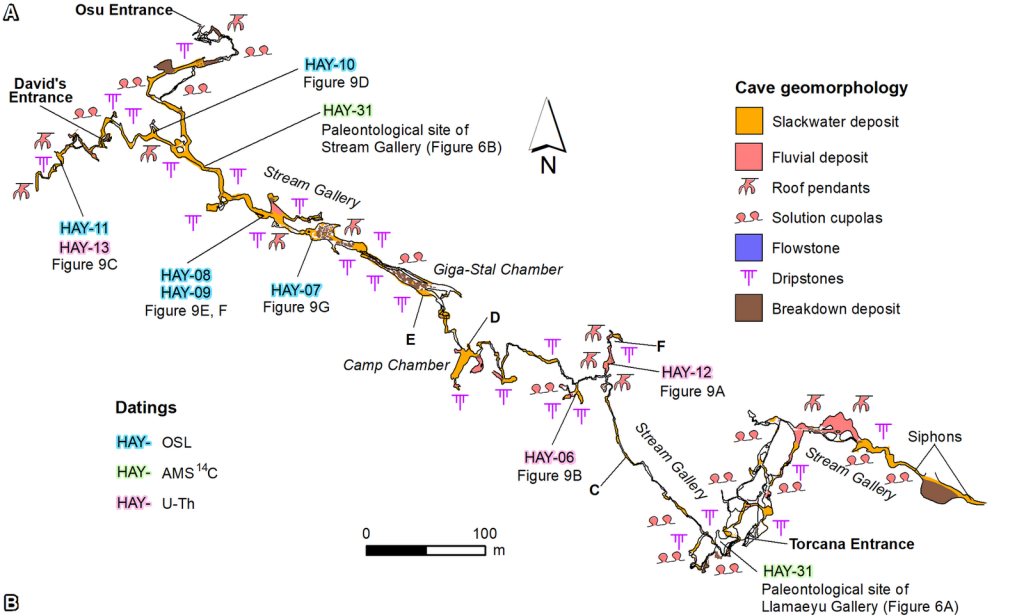
Glacial features

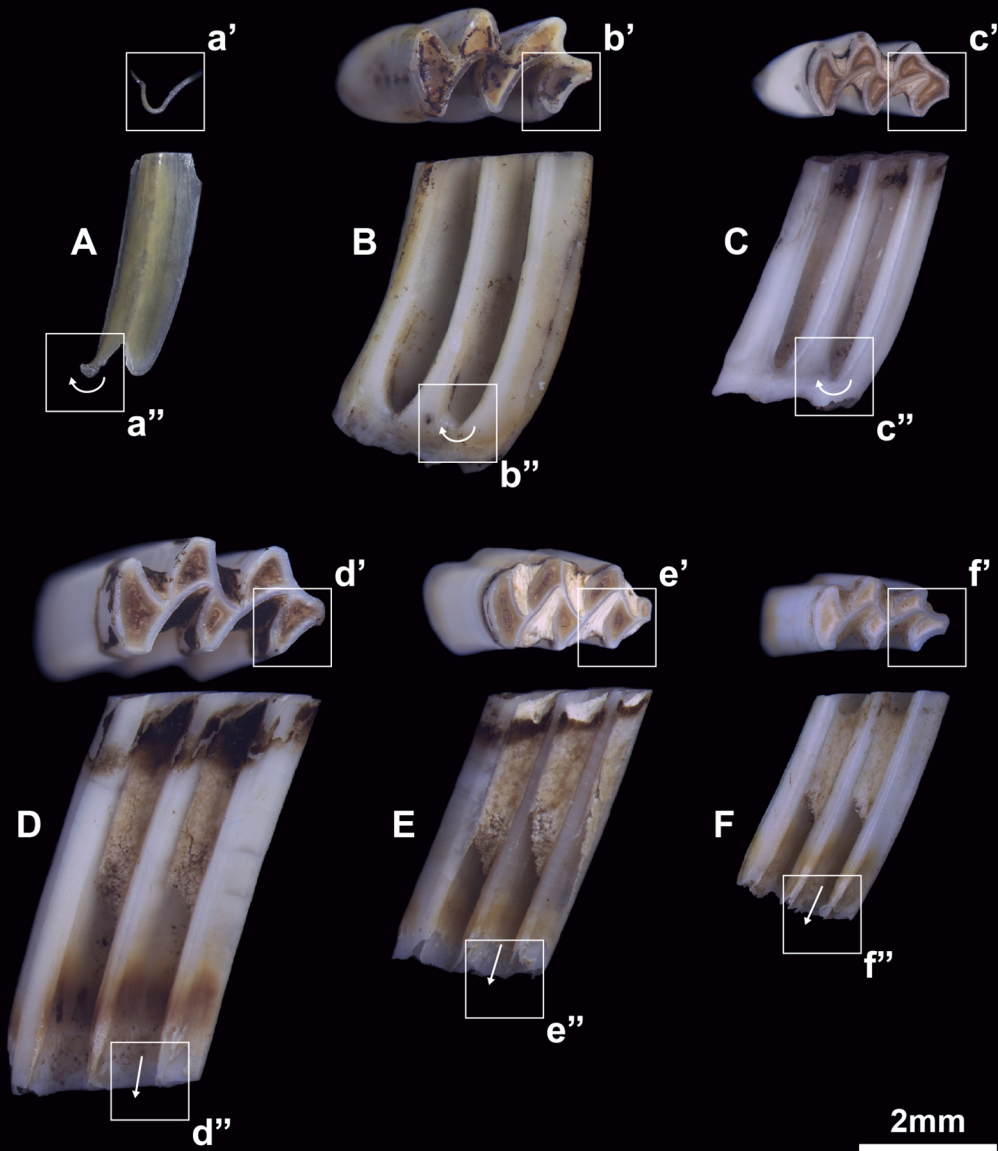
-  *Horn*
-  *Arête*
-  *Cirque*
-  Till

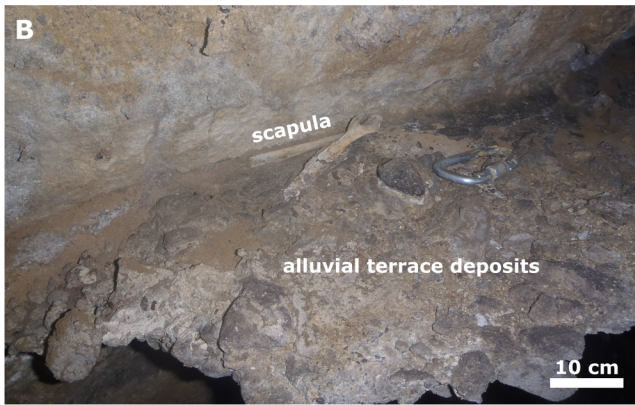
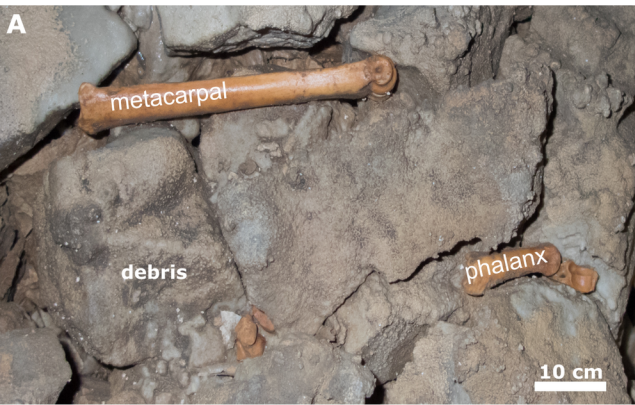
Other features

-  Glaciokarst closed depression
-  Slope deposit
-  Lacustrine, kame and peat and alluvial deposits
-  Anthropic deposit
-  River

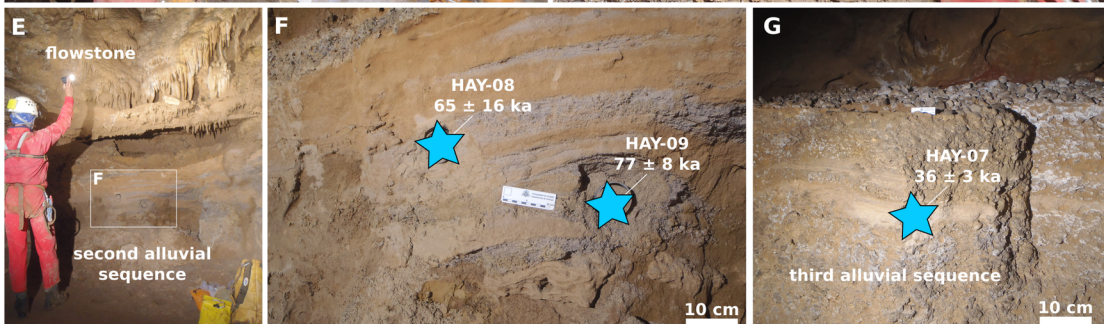
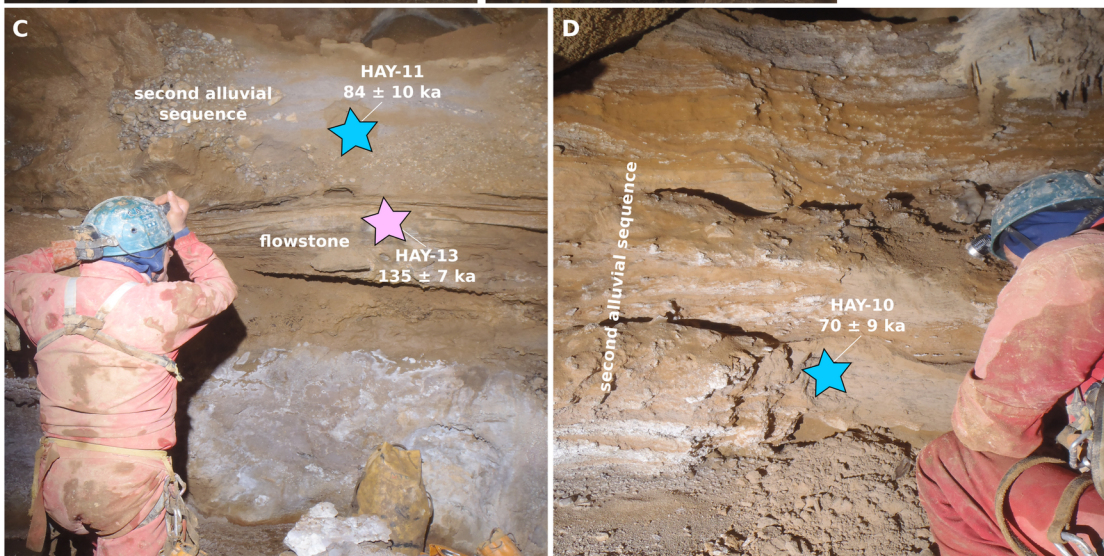
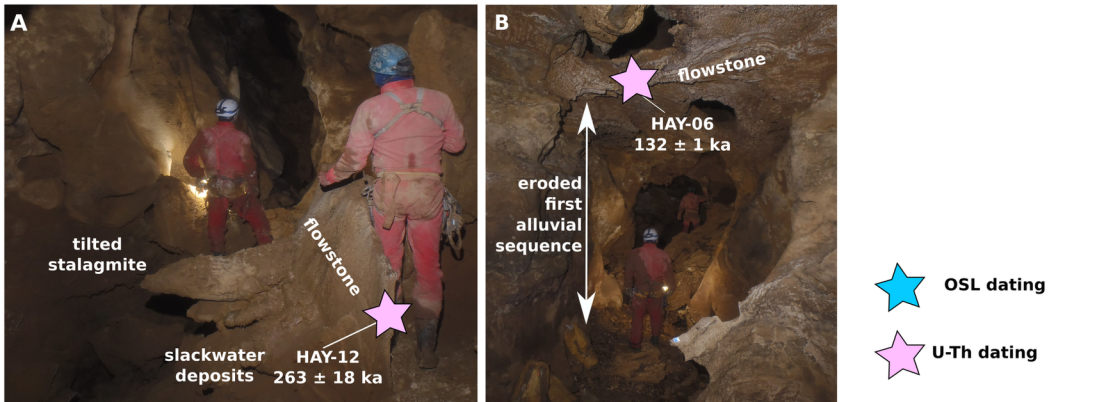


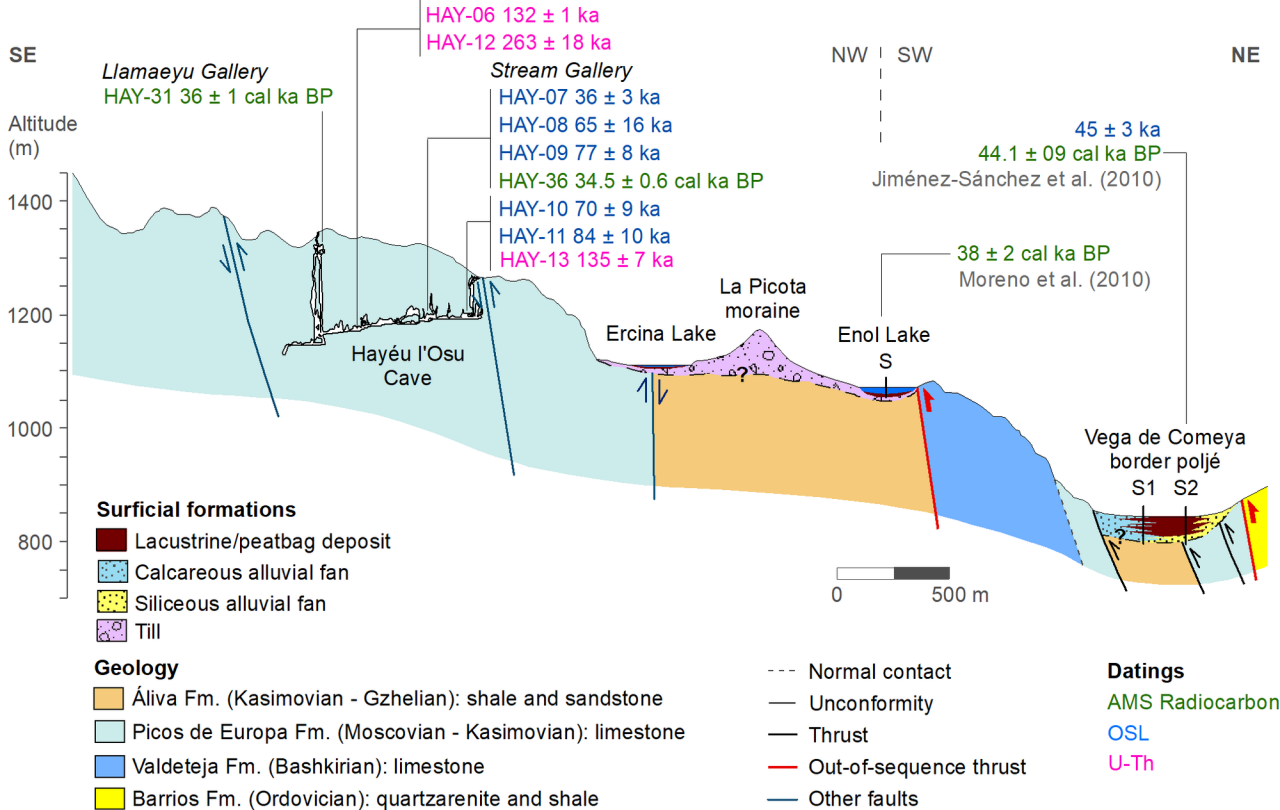












LGM
(?)

P
H
4

P
H
3

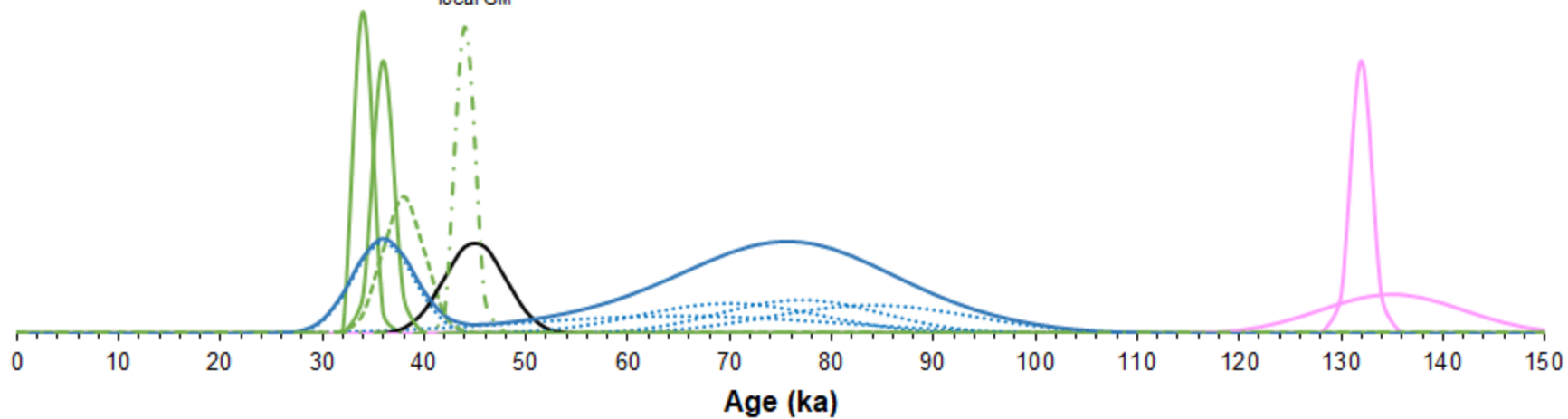
P
H
2

local GM

PH 1
Cave detrital sediment (MIS 4-5c)

MIS 5d
(?)

MIS 5e
Eemian



— Radiocarbon (bone)

- - - Radiocarbon - Enol Lake

- . - Radiocarbon - Vega de Comeya lacustrine infill

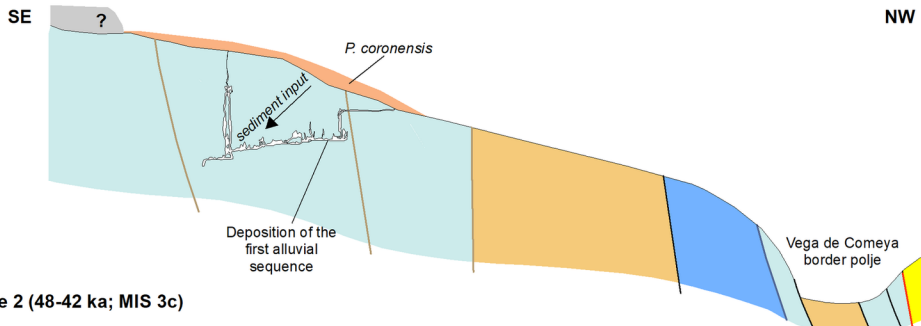
— U-Th (flowstone)

— OSL - Vega de Comeya lacustrine infill

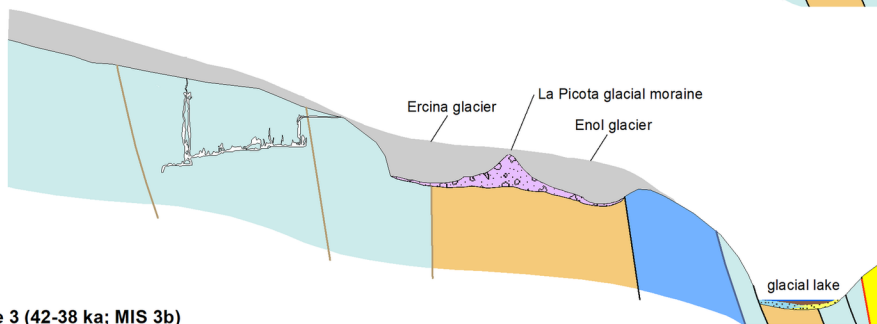
..... OSL (cave detrital sediment)

— OSL cum. (cave detrital sediment)

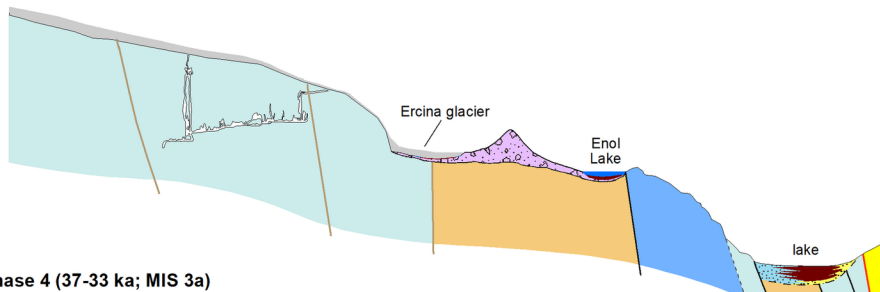
A Phase 1 (98-60 ka; MIS 5d-4)



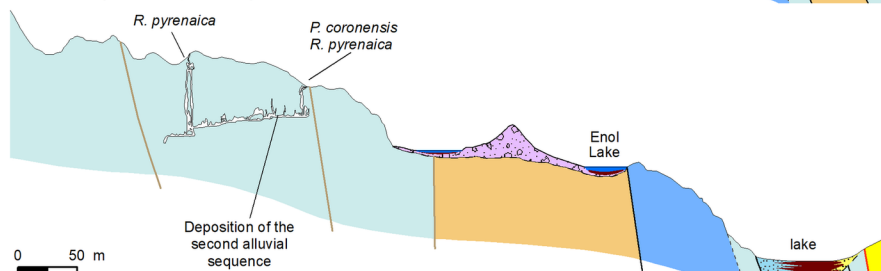
B Phase 2 (48-42 ka; MIS 3c)



C Phase 3 (42-38 ka; MIS 3b)



D Phase 4 (37-33 ka; MIS 3a)



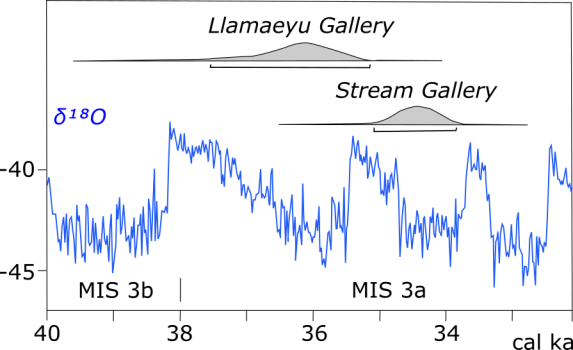


Table 1. ^{238}U - ^{230}Th dating results of Hayéu l'Osú Cave. The error is 2σ . Sample locations are shown in Figures 4A and 8A-C.

Sample	^{238}U (ppb)		^{232}Th (ppt)		$^{230}\text{Th} / ^{232}\text{Th}$ (atomic $\cdot 10^{-6}$)		$\delta^{234}\text{U}^*$ (measured)		$^{230}\text{Th} / ^{238}\text{U}$ (activity)		^{230}Th Age (yr) (uncorrected)		$\delta^{234}\text{U}_{\text{Initial}}^{**}$ (corrected)		^{230}Th Age (yr BP) *** (corrected)	
HAY-6	65.4	± 0.1	8643	± 173	293	± 6	1994.3	± 3.5	2.3433	± 0.0072	132630	± 732	2892	± 10	131570	± 1010
HAY-12	28.2	± 0.0	48898	± 980	16	± 0	644.1	± 3.4	1.7072	± 0.0068	286442	± 4903	1353	± 68	262977	± 17735
HAY-13	95.4	± 0.3	66643	± 1342	34	± 1	793.4	± 5.1	1.4240	± 0.0063	144811	± 1451	1161	± 24	134982	± 7103

* $\delta^{234}\text{U} = ([^{234}\text{U}/^{238}\text{U}]_{\text{activity}} - 1) \cdot 1000$. ** $\delta^{234}\text{U}_{\text{Initial}}$ was calculated based on the ^{230}Th age (T), i.e., $\delta^{234}\text{U}_{\text{Initial}} = \delta^{234}\text{U}_{\text{measured}} \cdot e^{\lambda_{234} \cdot T}$. Corrected ^{230}Th ages assume the initial $^{230}\text{Th}/^{232}\text{Th}$ atomic ratio of $4.4 \pm 2.2 \cdot 10^{-6}$. Those are the values for a material at secular equilibrium, with the bulk Earth $^{232}\text{Th}/^{238}\text{U}$ value of 3.8. The errors are arbitrarily assumed to be 50%. *** B.P. stands for “Before Present” where the “Present” is defined as the year 1950 A.D.

Table 2. Optically Stimulated Luminescence (OSL) dates from alluvial sandy sediment samples of Hayéu l'Osu Cave. Figures 4A, 8 and 9C-G show the position of the samples in the study cave.

Sample	HAY-07	HAY-08	HAY-09	HAY-10	HAY-11
Aliquots (n)	28	4	35	32	35
Equivalent doses (ED) (Gy)	48.4 ± 3.4	35.2 ± 8.4	47.8 ± 3.4	38.3 ± 2.8	44.3 ± 4.3
⁴⁰ K (Bq kg ⁻¹)	393 ± 13	50 ± 12	79 ± 17	71 ± 14	55 ± 9
²³⁸ U (Bq kg ⁻¹)	17 ± 2	18 ± 1	15.6 ± 0.8	18 ± 2	15 ± 2
²³⁵ U (Bq kg ⁻¹)	0 ± 0	0 ± 0	0 ± 0	0 ± 0	3.3 ± 2
²³² Th (Bq kg ⁻¹)	3.3 ± 0.5	0 ± 0	5.5 ± 0.8	0 ± 0	0 ± 0
Beta radiation dose	0.89 ± 0.04	0.31 ± 0.04	0.35 ± 0.04	0.31 ± 0.04	0.29 ± 0.04
Gamma radiation dose	0.39 ± 0.02	0.17 ± 0.01	0.21 ± 0.02	0.16 ± 0.02	0.17 ± 0.01
Cosmic radiation dose	0.06 ± 0.003	0.06 ± 0.003	0.06 ± 0.003	0.07 ± 0.003	0.07 ± 0.003
Dose rate (DR) (Gy ka ⁻¹)	1.34 ± 0.4	0.54 ± 0.04	0.62 ± 0.05	0.55 ± 0.06	0.53 ± 0.04
Overdispersion (%)	26.3 ± 5.8	38.9 ± 20.0	24.3 ± 5.5	26.1 ± 6.4	38.8 ± 8.7
Age (ka)	36 ± 3	65 ± 16	77 ± 8	70 ± 9	84 ± 10

Table 3. Calibrated AMS radiocarbon dates of chamois (*R. pyrenaica*) assemblage of Hayéu l'Osu Cave.

The position and remains of the paleontological sites is shown in Figures 4A, 7 and 8.

Sample	Paleontological sites	Conventional age (years BP)	Calendar age (2 σ) (years BP)
HAY-31	Stream Gallery	32220 \pm 440	37534–35139
HAY-36	Llamayeu Gallery	30440 \pm 360	35076–33836

Table 4. Synthesis of the paleoenvironmental evolution of Picos de Europe during MIS 5c to 3. See Section 5 and Figures 10 and 11 for details.

Phase	Age (ka)	MIS	Main event	Paleoenvironment at a reference altitude of 1400 m	Evidence from the study cave	Evidence from previous works
1	98-60	5c-4	Glacier retreat	Area with rocky outcrops and fluvioglacial sediments. Probably glaciers in upper areas. Relative cold conditions	Deposition of the second alluvial sequence in the cave Occurrence of <i>Pliomys coronensis</i>	
2	48-42	3c	Local glacial maximum advance	Area covered by glaciers		Glacio-lacustrine sedimentation in Vega de Comeya border polje at 850 m asl (Jiménez-Sánchez et al., 2013)
3	42-38	3b	Onset of glacier retreat	Probably, area covered by glaciers		Glacio-lacustrine sedimentation at Enol Lake at 1075 m asl (Moreno et al., 2009)
4	37-33	3a	Glacier retreat	Area with rocky outcrops and fluvioglacial sediments; relative cold conditions	Deposition of the third alluvial sequence in the cave Occurrence of <i>Rupicapra pyrenaica</i>	